The Astrophysical Journal, 904:51 (20pp), 2020 November 20 https://doi.org/10.3847/1538-4357/abbb96

Testing the Strong Equivalence Principle: Detection of the External Field Effect in Rotationally Supported Galaxies

Kyu-Hyun Chae[1], Federico Lelli[2], Harry Desmond[3], Stacy S. McGaugh[4], Pengfei Li[4], and James M. Schombert[5]
[1] Department of Physics and Astronomy, Sejong University, 209 Neungdong-ro Gwangjin-gu, Seoul 05006, Republic of Korea; chae@sejong.ac.kr, kyuhyunchae@gmail.com
[2] School of Physics and Astronomy, Cardiff University, Queens Buildings, The Parade, Cardiff, CF24 3AA, UK; LelliF@cardiff.ac.uk
[3] Astrophysics, University of Oxford, Denys Wilkinson Building, Keble Road, Oxford, OX1 3RH, UK; harry.desmond@physics.ox.ac.uk
[4] Department of Astronomy, Case Western Reserve University, Cleveland, OH 44106, USA; ssm69@case.edu, pxl283@case.edu
[5] Department of Physics, University of Oregon, Eugene, OR 97403, USA; jschombe@gmail.com
Received 2020 July 21; revised 2020 September 17; accepted 2020 September 23; published 2020 November 20

Abstract

The strong equivalence principle (SEP) distinguishes general relativity (GR) from other viable theories of gravity. The SEP demands that the internal dynamics of a self-gravitating system under freefall in an external gravitational field should not depend on the external field strength. We test the SEP by investigating the external field effect (EFE) in Milgromian dynamics (MOND), proposed as an alternative to dark matter in interpreting galactic kinematics. We report a detection of this EFE using galaxies from the Spitzer Photometry and Accurate Rotation Curves (SPARC) sample together with estimates of the large-scale external gravitational field from an all-sky galaxy catalog. Our detection is threefold: (1) the EFE is individually detected at 8σ to 11σ in "golden" galaxies subjected to exceptionally strong external fields, while it is not detected in exceptionally isolated galaxies, (2) the EFE is statistically detected at more than 4σ from a blind test of 153 SPARC rotating galaxies, giving a mean value of the external field consistent with an independent estimate from the galaxies' environments, and (3) we detect a systematic downward trend in the weak gravity part of the radial acceleration relation at the right acceleration predicted by the EFE of the MOND modified gravity. Tidal effects from neighboring galaxies in the Λ cold dark matter (CDM) context are not strong enough to explain these phenomena. They are not predicted by existing ΛCDM models of galaxy formation and evolution, adding a new small-scale challenge to the ΛCDM paradigm. Our results point to a breakdown of the SEP, supporting modified gravity theories beyond GR.

Unified Astronomy Thesaurus concepts: Non-standard theories of gravity (1118); Disk galaxies (391); Gravitation (661); Modified Newtonian dynamics (1069)

1. Introduction

The hypothesis that general relativity (GR) and its Newtonian limit hold exactly in the weak gravity regime requires that the universe is permeated by invisible dark matter (DM). The existence of DM is a key assumption of the standard cosmological model Λ cold dark matter (ΛCDM), which has been successful in explaining many cosmological observations on the largest scales of the cosmos (Frenk & White 2012; Peebles 2012). The ΛCDM paradigm, however, is facing several challenges on small scales (Kroupa 2015; Bullock & Boylan-Kolchin 2017), such as the unexpected phase-space correlation of satellite galaxies ("the satellite plane problem"; see, e.g., Kroupa et al. 2010; Müller et al. 2018) and the unexpected coupling in galaxies between the visible matter (baryons) and the observed dynamics, usually dominated by the DM halo at large radii (McGaugh et al. 2016; Lelli et al. 2017).

A drastically different idea is represented by the Milgromian dynamics (MOND) paradigm (Milgrom 1983) that modifies the standard laws of dynamics at low accelerations (weak gravitational fields) rather than assuming nonbaryonic DM. Several a priori predictions of MOND have been confirmed by later observations as reviewed by Sanders & McGaugh (2002), Famaey & McGaugh (2012), and McGaugh (2020). The construction of a MOND cosmology remains a tall order (McGaugh 2015), but the recent relativistic MOND theory of Skordis & Złośnik (2020) appears promising, being able to reproduce the power spectrum of the cosmic microwave background as good as ΛCDM.

The relativistic theory of Skordis & Złośnik (2020) reduces to the nonrelativistic modified-gravity theory of Bekenstein & Milgrom (1984), violating the strong equivalence principle (SEP) of GR: the internal dynamics of a self-gravitating body may be affected by external gravitational fields, beyond usual tidal forces. More specifically, these theories violate local positional invariance (LPI) for gravitational experiments, which differentiates the SEP from the less stringent (but well tested) Einstein equivalence principle, containing the weak equivalence principle, Lorentz invariance, and the LPI for nongravitational experiments only (Will 2014).

The radial acceleration relation (RAR) is of particular importance in the DM versus MOND debate (McGaugh et al. 2016; Lelli et al. 2017). This empirical relationship links the observed centripetal acceleration $g_{\rm obs}(R) = V_{\rm rot}^2(R)/R$ in galaxies to the expected Newtonian acceleration $g_{\rm bar}(R) = V_{\rm bar}^2(R)/R$ from the observed baryonic matter distribution:

$$g_{\rm obs} = \nu_0\left(\frac{g_{\rm bar}}{g_\dagger}\right)g_{\rm bar}, \quad (1)$$

where $\nu_0(z)$ is an empirical fitting function and $g_\dagger$ is an acceleration scale. In ΛCDM the RAR must arise from the

haphazard process of galaxy formation (Di Cintio & Lelli 2016; Desmond 2017; Keller & Wadsley 2017; Navarro et al. 2017), and $g_\dagger$ is an emergent scale that may (Ludlow et al. 2017) or may not (Tenneti et al. 2018) appear in cosmological simulations. In MOND $g_\dagger$ is a new universal constant of nature indicated as a_0 (Milgrom 1983), while the function $\nu_0(g_{\rm bar}/a_0)$ interpolates between the classic Newtonian regime $g_{\rm obs} = g_{\rm bar}$ at high accelerations and the Milgromian regime $g_{\rm obs} = \sqrt{g_{\rm bar} a_0}$ at low accelerations.

While the extrapolation of Equation (1) to large radii implies asymptotically flat rotation curves for isolated galaxies, MOND modified gravity (Bekenstein & Milgrom 1984) predicts that galaxies in strong external fields should display a weak but distinctive decline in their outer rotation curves. This peculiar feature, linking the internal dynamics on scales smaller than 100 kpc with the cosmological environment on scales of a few megaparsecs, can be used to distinguish between modified gravity in MOND and standard gravity with DM. Signatures of this external field effect (EFE) have been searched for in rotationally supported galaxies (Lelli et al. 2015; Wu & Kroupa 2015; Haghi et al. 2016) without conclusive and unambiguous evidence.

The EFE has also been investigated in pressure-supported stellar systems. Dwarf satellites of the Andromeda galaxy revealed some EFE signatures as predicted and tested by McGaugh & Milgrom (2013a, 2013b), but the possibility of tidal interactions and out-of-equilibrium dynamics complicates the interpretation (e.g., McGaugh & Wolf 2010; Lelli et al. 2017). Several authors (Famaey et al. 2018; Kroupa et al. 2018; Haghi et al. 2019; Müller et al. 2019) proposed MOND models incorporating the EFE to explain unexpectedly low stellar velocity dispersions of a few ultradiffuse galaxies. Globular clusters (GCs) of the Milky Way are dynamical systems subjected to external fields. MONDian kinematics for the GCs were predicted (Baumgardt et al. 2005; Haghi et al. 2009, 2011), but analyses of the observed data did not result in unambiguous signatures of the MOND EFE (Jordi et al. 2009; Frank et al. 2012).

Wide binary stars have also been used to test MOND and the EFE, with conflicting results (Hernandez et al. 2012, 2019; Pittordis & Sutherland 2019). In particular, wide binary stars from Gaia DR2 have been used to argue both for (Pittordis & Sutherland 2019) and against (Hernandez et al. 2019) the presence of the EFE, and further studies are required to provide conclusive evidence.

Here we report a robust EFE detection in rotationally supported galaxies using two complementary approaches: (1) focusing on individual galaxies where the external gravitational field is exceptionally large, and (2) studying weak systematic deviations from the RAR driven by the mean gravitational field of the local universe. Throughout we take $g_\dagger = 1.2 \times 10^{-10}$ m s^{-2} (McGaugh et al. 2016; Lelli et al. 2017) and use the notation $x \equiv \log_{10}(g_{\rm bar}/{\rm m\ s^{-2}})$ and $y \equiv \log_{10}(g_{\rm obs}/{\rm m\ s^{-2}})$.

2. Data and Methodology

2.1. The SPARC Database

The Spitzer Photometry and Accurate Rotation Curves (SPARC) database (Lelli et al. 2016) contains 175 rotationally supported galaxies in the nearby universe.[6] These galaxies have stellar masses ranging from $M_\star \simeq 10^{11} M_\odot$ to $M_\star \simeq 10^7 M_\odot$ and cover all Hubble types of late-type, star-forming galaxies, including low-surface-brightness disk galaxies. The database provides the observed rotation velocities ($V_{\rm obs}$) from spatially resolved H I observations and the Newtonian circular velocities from the observed distribution of stars and gas. The latter include the stellar disk contribution ($V_{\rm disk}$) and (if present) the bulge contribution ($V_{\rm bul}$) for a baseline mass-to-light ratio of unity, as well as the gas contribution ($V_{\rm gas}$) for a total-to-hydrogen mass ratio of 1.33. For convenience, in this paper we redefine $V_{\rm gas}$ for a total-to-hydrogen mass ratio of unity. The reported velocity $V_{\rm obs}$ of a galaxy is tied to the reported inclination $i_{\rm obs}$. If the inclination is changed to i, the rotation velocity becomes

$$V_{\rm rot} = V_{\rm obs} \frac{\sin(i_{\rm obs})}{\sin(i)}. \tag{2}$$

The circular velocity due to the baryonic mass distribution depends on the galaxy distance D and is given by

$$V_{\rm bar} = \sqrt{\hat{D}(\Upsilon_{\rm disk} V_{\rm disk}^2 + \Upsilon_{\rm bul} V_{\rm bul}^2 + \Upsilon_{\rm gas} V_{\rm gas}|V_{\rm gas}|)}, \tag{3}$$

where $\hat{D} \equiv D/D_{\rm obs}$ with $D_{\rm obs}$ being the fiducial distance. In Equation (3), $\Upsilon_{\rm disk}$ and $\Upsilon_{\rm bul}$ are the mass-to-light ratios of the disk and the bulge in units of the solar value $M_\odot/L_\odot$ at 3.6 μm, while $\Upsilon_{\rm gas}$ is the ratio of the total gas mass to the H I mass. When the SPARC database was published, this ratio was assumed to be 1.33 to account for the cosmic abundance of helium from Big Bang nucleosynthesis. Here we consider the small amounts of helium and metals formed via stellar nucleosynthesis during galaxy evolution (McGaugh et al. 2020), so that $\Upsilon_{\rm gas} = X^{-1}$ where X is a function of stellar mass ($M_\star$):

$$X = 0.75\text{–}38.2\left(\frac{M_\star}{M_0}\right)^\alpha, \tag{4}$$

with $M_0 = 1.5 \times 10^{24} M_\odot$ and $\alpha = 0.22$. We do however allow the possibility of varying $\Upsilon_{\rm gas}$ from X^{-1} to consider the uncertainties in the H I flux, gas disk geometry, and the gas mass to H I mass ratio. In some cases $V_{\rm gas}$ is negative at small radii, representing the fact that the Newtonian gravitational field is not oriented toward the center when a large fraction of the gas disk lies in the outer regions. To account for the cases of negative $V_{\rm gas}$ we write $V_{\rm gas}|V_{\rm gas}|$ rather than $V_{\rm gas}^2$ in the last term of Equation (3), although this detail has negligible effects on our study.

2.2. The External Field Effect

Empirically, the observed centripetal acceleration ($g_{\rm obs} = V_{\rm obs}^2/R$) is related to the Newtonian baryonic acceleration ($g_{\rm bar} = V_{\rm bar}^2/R$) via the RAR $\nu_0(g_{\rm bar}/g_\dagger)$ of Equation (1) with a free parameter $g_\dagger$ (McGaugh et al. 2016; Lelli et al. 2017). In a MOND framework, $g_\dagger = a_0$ is a fundamental constant of nature (Milgrom 1983) and Equation (1) can be obtained by modifying either inertia (Newton's second law of dynamics) or gravity (Poisson's equation) at the nonrelativistic level (Famaey & McGaugh 2012). In MOND modified-inertia theories Equation (1) holds exactly for any circular orbit (Milgrom 1994), while in MOND modified-gravity theories holds only for highly symmetric mass distributions (such as

[6] http://astroweb.cwru.edu/SPARC/

spheres) and represents a first-order approximation for actual disk galaxies (Brada & Milgrom 1995). In all these scenarios, however, Equation (1) is strictly valid only for isolated systems, when the EFE is negligible.

To build a general fitting function that approximates the EFE, we start from the nonlinear MOND modified Poisson's equation (Bekenstein & Milgrom 1984) in the one-dimensional case. If we assume a uniform external gravitational field $g_{\rm ext}$ (Famaey & McGaugh 2012) and the so-called Simple interpolating function (IF; Famaey & Binney 2005), we have

$$g_{\rm MOND}(R) = \nu_e\left(\frac{g_{\rm bar}}{g_\dagger}\right) g_{\rm bar}(R) \tag{5}$$

with

$$\nu_e(z) = \frac{1}{2} - \frac{A_e}{z} + \sqrt{\left(\frac{1}{2} - \frac{A_e}{z}\right)^2 + \frac{B_e}{z}}, \tag{6}$$

where $z \equiv g_{\rm bar}/g_\dagger$, $A_e \equiv e(1 + e/2)/(1 + e)$, $B_e \equiv (1 + e)$, and $e \equiv g_{\rm ext}/g_\dagger$. For $e = 0$, $\nu_e(z)$ is reduced to the Simple IF $\nu_0(z) = 1/2 + \sqrt{1/4 + 1/z}$. Equation (6) is based on the footnote to Equation (59) of Famaey & McGaugh (2012), but we corrected a small typo and rearranged it. Note here that the Simple IF allows the convenient analytic form of Equation (6) with $e > 0$ while it is only subtly different (Chae et al. 2019) in the (EFE-irrelevant) high acceleration limit from the function used by McGaugh et al. (2016) and Lelli et al. (2017) to fit the SPARC galaxies. Our results on the EFE detection are not affected by the choice of the Simple IF. Then, the expected circular velocity is given by

$$V_{\rm MOND}(R) = \sqrt{\nu_e\left(\frac{g_{\rm bar}}{g_\dagger}\right)} V_{\rm bar}(R). \tag{7}$$

Although $\nu_e(z)$ (Equation (6)) is based on idealized assumptions, it captures the basic feature of the EFE: a systematic downward deviation from $\nu_0(z)$ (Equation (1)) when $e > 0$ as $z \to 0$. Equation (6) also allows for upward deviations when $e < 0$, which seem unphysical but may be preferred by the data at the empirical level. These features are illustrated in Figure 1. MOND with the EFE predicts that the RAR must be a family of functions rather than a universal function. This also means that if galaxies in different environments are tried to be fitted with a single functional form of Equation (1), then there will arise some small intrinsic scatter of $g_\dagger$ due to the EFE. Most importantly, regardless of its MOND origin, Equation (6) may be considered a mere fitting function that improves over Equation (1) by adding the free parameter e, which has no a priori knowledge of the external gravitational field in which galaxies reside.

2.3. MCMC Simulations

In our Bayesian analysis the posterior probability of parameters $\boldsymbol{\beta} = \{\beta_k\}$ is defined by

$$p(\boldsymbol{\beta}) \propto \exp\left(-\frac{\chi^2}{2}\right) \prod_k \Pr(\beta_k), \tag{8}$$

where $\Pr(\beta_k)$ is the prior probability of parameter β_k and χ^2 is given by

$$\chi^2 = \sum_{j=1}^{N} \left(\frac{V_{\rm rot}(R_j) - V_{\rm MOND}(\boldsymbol{\beta}; R_j)}{\sigma_{V_{\rm rot}(R_j)}}\right)^2, \tag{9}$$

with $\sigma_{V_{\rm rot}(R_j)} = \sigma_{V_{\rm obs}(R_j)} \sin(i_{\rm obs})/\sin(i)$ where $\sigma_{V_{\rm obs}(R_j)}$ is the reported error of $V_{\rm obs}(R_j)$ for the reported inclination $i_{\rm obs}$. As in earlier studies of the RAR using SPARC galaxies (McGaugh et al. 2016; Lelli et al. 2017), we use only 153 galaxies with $i_{\rm obs} \geqslant 30^\circ$ and $Q \leqslant 2$ (a quality cut on the rotation curve).

The parameters $\boldsymbol{\beta}$ in Equation (8) are given by $\boldsymbol{\beta} = \{\Upsilon_{\rm disk}, \Upsilon_{\rm bul}, \Upsilon_{\rm gas}, \hat{D}, i, e\}$ for the case of using Equation (5) with a fixed $g_\dagger = 1.2 \times 10^{-10}$ m s^{-2}. The priors on these parameters are summarized in Table 1. The mean values and standard deviations of $\Upsilon_{\rm disk}$ and $\Upsilon_{\rm bul}$ are motivated by state-of-the-art stellar population synthesis models for star-forming galaxies (Schombert et al. 2019). The mean value of $\Upsilon_{\rm gas}$ is given by Equation (4), while the standard deviation is motivated by the typical error on the H I flux calibration, but it could also represent variations in the assumed gas disk thickness and/or the mean gas-to-H I mass ratio. The mean values and standard deviations of $\hat{D}$ and i consider the baseline SPARC values and their fiducial errors. For e we adopt an uninformative uniform prior covering a reasonably broad range.

The posterior probability density functions (PDFs) of the model parameters are derived from Markov Chain Monte Carlo (MCMC) simulations through the public code `emcee` (Foreman-Mackey et al. 2013). These simulations represent an extension to the previous SPARC analysis (Li et al. 2018) including the EFE parameter e. We choose $N_{\rm walkers} = 10{,}000$ and $N_{\rm iteration} = 6000$. We discard models up to $N_{\rm iteration} = 500$ and thin the rest by a factor of 50 as the autocorrelation lengths for the parameters are <100. The posterior PDFs of $x = \log_{10} g_{\rm bar}(R)$ and $y = \log_{10} g_{\rm MOND}(R)$ follow from the posterior PDFs of the parameters i, $\log_{10}\hat{D}$, $\log_{10}\Upsilon_{\rm disk}$, $\log_{10}\Upsilon_{\rm bul}$, and $\log_{10}\Upsilon_{\rm gas}$.

2.4. The Environmental Gravitational Field

We estimate the environmental gravitational field $g_{\rm env}$ due to the large-scale distribution of matter at the positions of the SPARC galaxies. We perform this calculation within the standard ΛCDM context (Desmond et al. 2018). A similar calculation is not feasible in a MOND context due to the strong nonlinearities in the theory and the lack of a proper MOND cosmology. The ΛCDM calculation, however, is a good first-order approximation for MOND and other modified gravity theories (Desmond et al. 2018), up to some systematic uncertainty due to the unknown relation between $g_{\rm env}$ in these theories. We use $g_{\rm env}$ primarily for the purpose of picking out extreme cases with exceptionally high or low $g_{\rm env}$ (which should remain true in a relative sense in any cosmological scenario) and to check that the maximum-likelihood values of e from fitting Equation (5) are sensible in an order-of-magnitude fashion.

Our calculation of $g_{\rm env}$ starts with the total dynamical masses of the galaxies in the all-sky 2M++ survey (Lavaux & Hudson 2011) using abundance matching. We then use N-body simulations in ΛCDM to populate the surrounding regions with halos hosting galaxies too faint to be recorded in 2M++, using

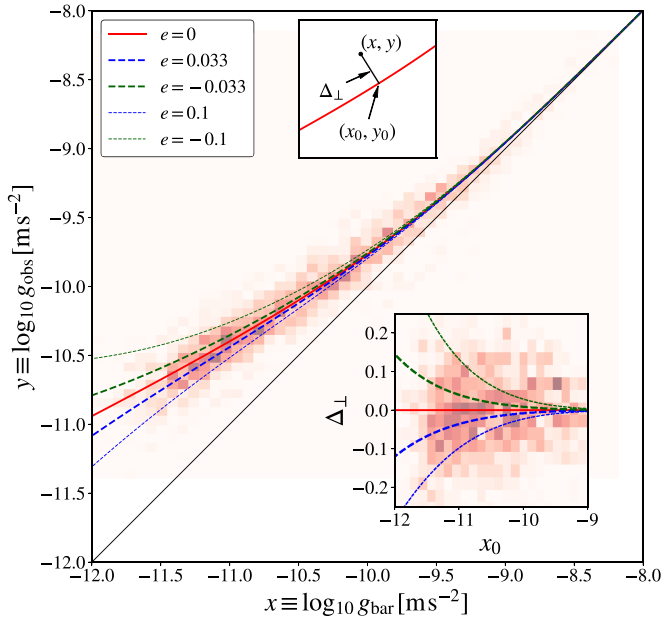

Figure 1. The external field effect in the weak-field limit of the radial acceleration relation. Equation (5) is overlaid on the RAR for various values of e in Equation (5). Values of $e > 0$ correspond to the MOND EFE, while $e < 0$ is unphysical from the MOND point of view. The value of $e \approx 0.033$ corresponds to the average prediction for 153 SPARC galaxies based on their gravitational environments (Desmond et al. 2018). The heat map shows the original SPARC mass models (Lelli et al. 2016) with fixed stellar mass-to-light ratios for the same galaxies.

Table 1
Summary of Prior Constraints on the Model Parameters

Parameter	Distribution	(μ, σ) or Range
$\Upsilon_{\rm disk}$	Lognormal	($\log_{10}(0.5)$, 0.1)
$\Upsilon_{\rm bul}$	Lognormal	($\log_{10}(0.7)$, 0.1)
$\Upsilon_{\rm gas}$	Lognormal	($\log_{10}(X^{-1})$, 0.04)
$\hat{D}$	Lognormal	(0, $\log_{10}(1 + \sigma_{D_{\rm obs}}/D_{\rm obs})$)
i	Gaussian	($i_{\rm obs}$, $\sigma_{i_{\rm obs}}$)
e	Uniform	[−0.5, 0.5]

statistical correlations between halo abundances and properties of the galaxy field. Finally, we add mass in long-wavelength modes of the density field according to the inferences of the BORG algorithm (Lavaux & Jasche 2016) applied to the 2M++ catalog. We use the final density field to calculate a posterior distribution for $g_{\rm env}$ at the position of each SPARC galaxy, fully propagating uncertainties in the input quantities. We define $e_{\rm env} \equiv g_{\rm env}/g_\dagger$, and find values in the range $0.01 \lesssim e_{\rm env} \lesssim 0.1$ with a mean of 0.033 among the SPARC galaxies: typical values are in the range 0.02–0.05.

3. Results

3.1. Individual Galaxies

The estimated values of the environmental gravitational field strength $e_{\rm env}$ (Section 2.4) span almost one order of magnitude, thus there is sufficient dynamic range to check whether or not the rotation-curve shapes depend on the large-scale environment. Among the SPARC galaxies whose rotation curves (RCs) reach $g_{\rm obs} < g_\dagger$, NGC 5033 and NGC 5055 live in exceptionally dense environments with $e_{\rm env} \approx 0.1$, while NGC 1090 and NGC 6674 are exceptionally isolated with $e_{\rm env} \approx 0.01$. The former two represent "golden galaxies" for the EFE to be detected, while the latter two are control targets for the null detection.

We fit the RCs using the EFE-incorporated RAR fitting function (Equation (5)) with a free external field $g_{\rm ext}$ parameterized by $e = g_{\rm ext}/g_\dagger$ (Section 2.2). The case of $e = 0$ implies flat RCs and reduces exactly to the original RAR (Equation (1)). Figure 2 shows the MCMC results for the RCs of four galaxies in the two extreme environments. The "corner" plots showing the posterior PDFs of the parameters for these galaxies can be found in Appendix A.

For NGC 5055, the detailed shape of the RC is very well fitted with a positive e but poorly fitted with $e = 0$. We find $e = 0.054 \pm 0.005$: this is an 11σ detection. Remarkably, this value is consistent within 2σ with $e_{\rm env} = 0.094^{+0.089}_{-0.022}$ that is independently determined from the large-scale environment. The Bayesian information criterion (BIC $\equiv -2 \ln L_{\rm max} + k \ln N$ where $L_{\rm max}$ is the maximum likelihood, k is the number of free parameters, and N is the number of the fitted rotation velocities) for $e = 0$ relative to the free e case is $\Delta{\rm BIC} = 144$, indicating very strong evidence for $e > 0$ based on the conventional criterion of $\Delta{\rm BIC} > 10$ for strong evidence.

For NGC 5033, the overall fit is also improved by freeing up e since $\Delta{\rm BIC} = 83.9$. We find $e = 0.104^{+0.013}_{-0.012}$. This is an 8σ detection, in excellent agreement with $e_{\rm env} = 0.102^{+0.086}_{-0.021}$ from the large-scale environment. The observed properties of this galaxy, however, are not as robust as those of NGC 5055. The rotation velocities at $R < 60''$ (about 5 kpc) are probably underestimated due to beam-smearing effects in the H I data, although our results on e are not affected by these data points. Moreover, while the distance of NGC 5055 is robust because it is based on the tip magnitude of the red giant branch ($D = 9.90 \pm 0.30$), that of NGC 5033 is very uncertain because it is estimated using Hubble flow models ($D = 15.70 \pm 4.70$). Interestingly, our MCMC result for NGC 5033 predicts a relatively large distance ($D = 23.5^{+2.0}_{-1.8}$ Mpc) with $e > 0$ but a low one ($D = 13.0^{+0.7}_{-0.6}$ Mpc) with $e = 0$. Hence, future observations can provide a key independent test.

In striking contrast to the highest $e_{\rm env}$ sample, the galaxies in the lowest $e_{\rm env}$ sample show no strong evidence for $e > 0$ based on $\Delta{\rm BIC}$ (or any other widely used statistic). These two galaxies are similar to the golden galaxies in morphology, mass, and size. The only noticeable difference is that they are unusually isolated. The fitted e values are consistent with the independent $e_{\rm env}$ values within about 2σ.

3.2. Statistical Approach

Since the EFE has subtle effects on rotation-curve shapes, positive values of e are detected with high statistical significance only in individual galaxies where $e_{\rm env}$ is exceptionally large (like NGC 5055 and NGC 5033). The EFE, however, should also imprint a statistical signature in the low-acceleration portion of the RAR (see Figure 1).

3.2.1. The Systematic Trend in the Low-acceleration Portion of the RAR

We use 153 galaxies from the SPARC database (Section 2.1). Figure 3 (top panels) shows the RAR for 2696 points having accuracy in $V_{\rm rot}$ better than 10%. In the top left panel we first

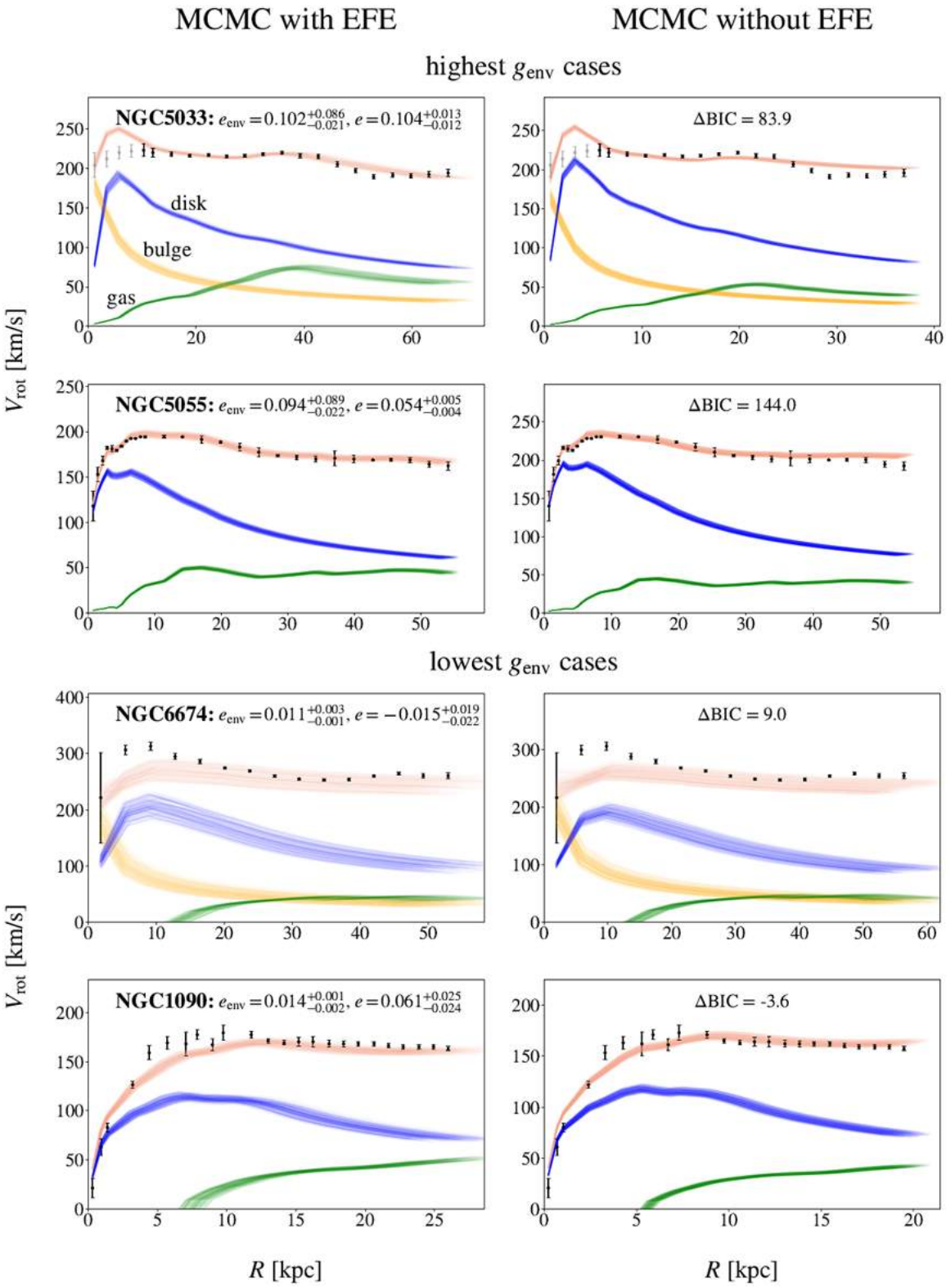

Figure 2. Detection of the EFE in individual galaxies. The observed rotation curves (points with error bars) are fitted using Equation (1) with no EFE (right panels) and a generalized equation considering the EFE (Equation (5)) (left panels). The colored bands show the 1σ confidence limits for the rotation curve (red) and the separate contributions of gas disk (green), stellar disk (blue), and stellar bulge (orange) if present. For the "golden galaxies" subjected to the strongest environmental gravitational fields, the fit is improved dramatically with $e > 0$, resulting in 11σ and 8σ individual detections of the EFE. For the galaxies subjected to the weakest fields, the EFE is not detected as expected. In all cases, the fitted values of e are fully consistent with the independent values of $e_{\rm env}$ from the large-scale galaxy environment within $\sim 2\sigma$. ΔBIC indicates evidence by the Bayesian Information Criterion.

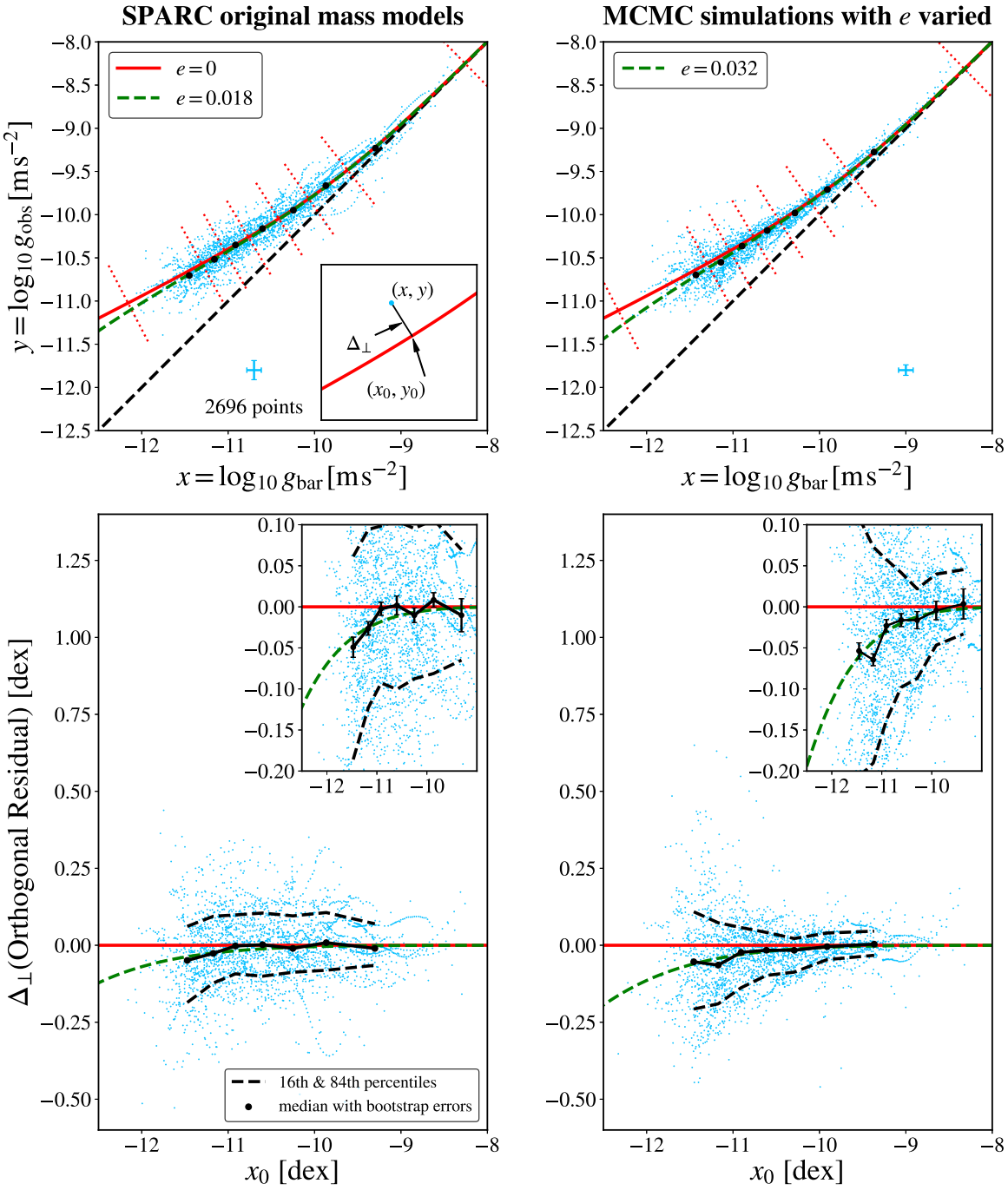

Figure 3. EFE detection in the low-acceleration portion of the RAR. In the top panels, the Newtonian acceleration from the baryons $g_{\rm bar}$ is plotted against the observed acceleration $g_{\rm obs}$ for a sample of 153 SPARC galaxies. The typical error bars are indicated in the bottom. The data are fitted using Equation (1) (red solid curve with $g_\dagger = 1.2 \times 10^{-10}$ m s^{-2}) corresponding to $e = 0$, and using the additional free parameter e accounting for the EFE (green dashed curve). The black dots show the median values within the bins orthogonal to Equation (1) (red dotted lines). The inset illustrates how orthogonal residuals are calculated. The bottom panels show the orthogonal residuals versus x_0: the deviation at $x_0 < -11$ represents a statistical detection of the EFE. The inset zooms into this interesting region. The left column shows the original SPARC mass models with fixed stellar mass-to-light ratios, while the right column shows the MCMC results with varied stellar mass-to-light ratios and considering the EFE. In both cases, the fitted e value is remarkably similar to $\langle e_{\rm env} \rangle \approx 0.033$ from the large-scale mass distribution in the nearby universe.

show the original SPARC mass models (Lelli et al. 2016) with fixed mass-to-light ratios at 3.6 μm of $\Upsilon_{\rm disk} = 0.5 M_\odot/L_\odot$ for the disk and $\Upsilon_{\rm bulge} = 0.7 M_\odot/L_\odot$ for the bulge (Lelli et al. 2017). The MCMC mass models obtained here with varied mass-to-light ratios (Section 2.3) are shown in the top right panel. We divide the data points into bins perpendicular to the best-fit curve assuming Equation (1). Each data point (x, y) is projected onto the point (x_0, y_0), so the orthogonal residual $\Delta_\perp$ encodes any possible systematic deviation from the $e = 0$ case.

The data show a small systematic deviation from Equation (1) for $x_0 \lesssim -11$. This trend is present, though weakly, in the original SPARC mass models with fixed mass-to-light ratios for the disks and bulges. The MCMC models in the middle column show a stronger effect. The systematic deviation is weak in absolute terms (0.05–0.08 dex for the lowest x_0 bin) but at least 4 times larger than the bootstrap error of the median in the bin. This demonstrates that Equation (1) does not fully capture the trends in the RAR. Introducing e as an additional free parameter, we obtain

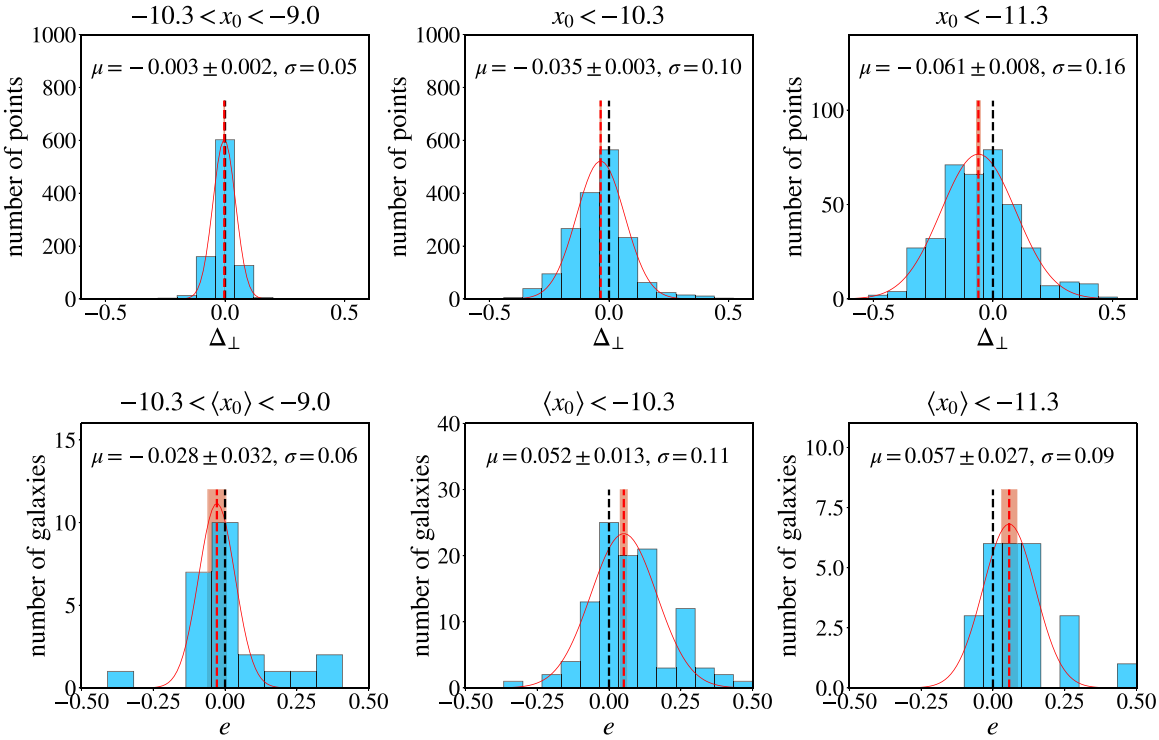

Figure 4. Distributions of $\Delta_\perp$ and e from fitting Equation (5) to the SPARC galaxies. The top panels show the distributions of orthogonal residuals $\Delta_\perp$ for three acceleration bins from the MCMC results shown in the middle column of Figure 3. The mean of the distribution is displaced from zero for lower acceleration bins, indicating declining RCs. The bottom panels show the distributions of the e values fitted to the individual galaxies binned by the median values of x_0 within the galaxies. As expected, for the galaxies in the high acceleration bin ($-10.3 < \langle x_0 \rangle < -9.0$), the data do not have any sensitivity to e and so the distribution has a mean of $\sim$0. For lower acceleration bins the distributions are shifted to positive e with high statistical significance, indicating a preference for the EFE. The broad distributions are due to the broad individual posteriors on e.

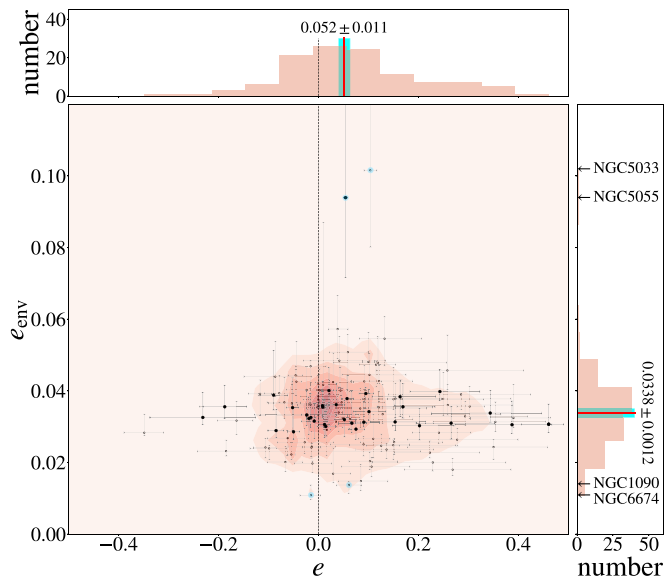

Figure 5. Statistical detection of the EFE. The median values of e from rotation-curve fits are compared with $e_{\rm env}$ values from the large-scale galaxy environment (Desmond et al. 2018) for 113 galaxies with $\langle x_0 \rangle < -10.3$. The heat map considers the posterior probabilities of individual e measurements. The distributions of e and $e_{\rm env}$ are shown by the top and right histograms. The median value of e is clearly offset from zero, indicating a 5σ statistical detection of the EFE. The value of $\langle e \rangle = 0.052 \pm 0.011$ is statistically consistent with $\langle e_{\rm env} \rangle = 0.034 \pm 0.001$ (see also Appendix B). The individual galaxies considered in Figure 2 are indicated: for the golden galaxies at exceptionally high $e_{\rm env}$ values, e is significantly different from zero at 8σ (NGC 5033) and 11σ (NGC 5055). Big dots indicate galaxies with accurate distances.

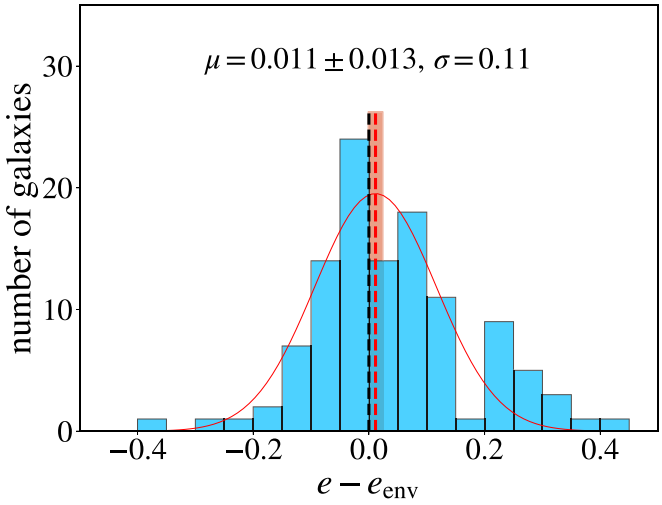

Figure 6. Comparison of external field strength estimates from kinematics vs. analyzing the galaxies' environments. The distribution of e derived from MCMC fits to the rotation curves is compared with that estimated from the observed environments of the galaxies ($e_{\rm env}$). There is good agreement up to the large uncertainties on the fitted values.

a better fit and find $e \approx 0.02$–0.04 in close agreement with the independent estimate of $\langle e_{\rm env} \rangle \simeq 0.033$ from an all-sky galaxy catalog (Section 2.4).

3.2.2. The Statistical Detection of the EFE

The systematic trend in the RAR also implies that the fitted individual values of e of Equation (5) will be systematically

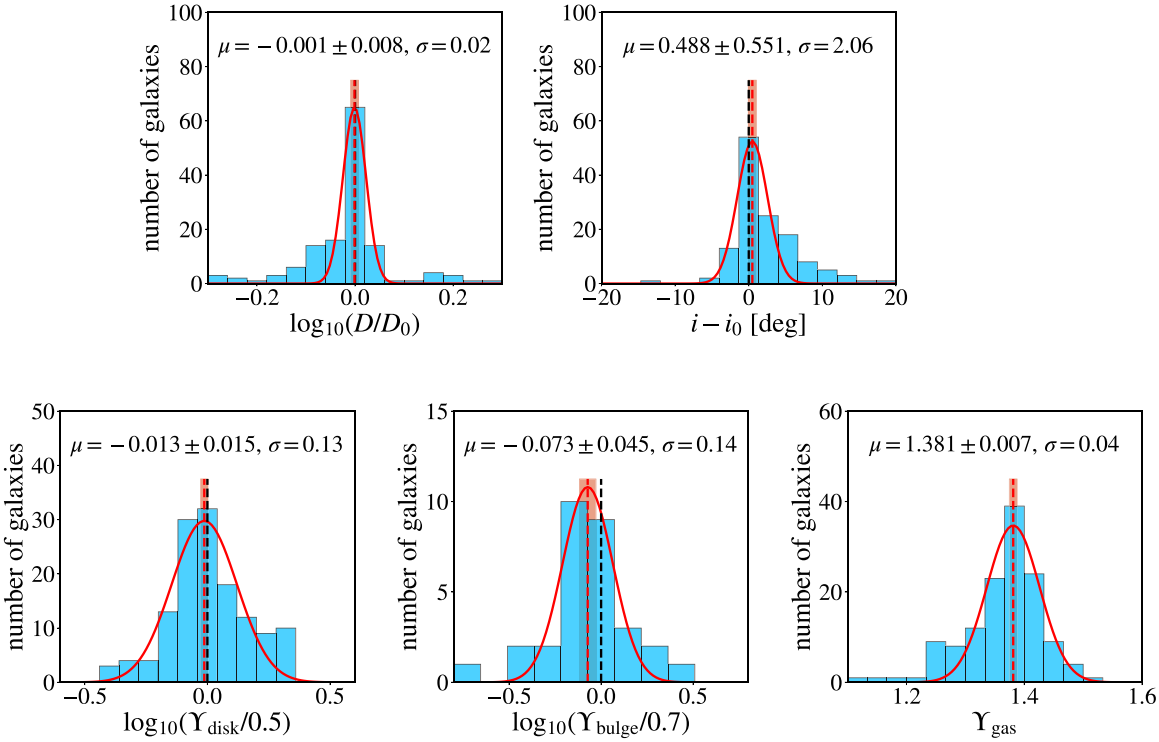

Figure 7. Fitted parameters for the 153 SPARC galaxies. The distributions of the fitted parameters from our MCMC simulations using Equation (5) are compared with the SPARC measured or assumed values.

displaced from the non-EFE case $e = 0$. The posterior PDFs of e are quite broad with a typical standard deviation of $\sim$0.04 (see Appendix A for examples). Nevertheless, the statistical distribution of the fitted values will have a signature. Because e was allowed to take any value (positive or negative), this distribution provides a blind test of MOND EFEs (Section 2.2).

Figure 4 shows the distribution of the orthogonal residual $\Delta_\perp$ and the fitted median value of e from the MCMC simulations with Equation (5). From Figure 1 it is expected that data points at high enough accelerations do not have any sensitivity to e. Indeed, for data points with $-10.3 < x_0 < -9$ the distribution of $\Delta_\perp$ gives a null result. Similarly, for galaxies with $-10.3 < \langle x_0 \rangle < -9$, the distribution of e (median value) gives a null result.

Data points at low enough accelerations will have sensitivity to e and distributions with nonzero mean value are expected from Figure 3. For data points with $x_0 < -11.3$ the distribution of $\Delta_\perp$ has a mean of -0.061 ± 0.008 (a bootstrap error) which is statistically significant at more than 7σ. For a much larger number of data points with $x_0 < -10.3$, $\Delta_\perp$ has a smaller deviation of -0.035 ± 0.003, but the statistical significance of the deviation is more than 11σ.

Figure 5 shows individual e values and their uncertainties for a subset of 113 galaxies with median $\langle x_0 \rangle < -10.3$. Due to the large uncertainties on e, some galaxies can occasionally return negative values. However, the median value of e is 0.052 ± 0.011 (bootstrap error), which represents $\approx 5\sigma$ detection of positive e. This value is statistically consistent with the median environmental gravitational field for these galaxies ($\langle e_{\rm env} \rangle = 0.034 \pm 0.001$ (bootstrap error)). Furthermore, based on the robust binomial statistic with equal probabilities for $e > 0$ and $e < 0$, 78 cases of $e > 0$ out of 113 is 4σ away from the expected mean of 56.5 cases.

Figure 6 further shows the distribution of the individual difference $e - e_{\rm env}$. It has a broad distribution due to the large uncertainty in e but is clearly consistent with zero: $\langle e - e_{\rm env} \rangle = 0.011 \pm 0.013$. It is intriguing that the mere fitting parameter e returns, on average, the same value of the mean environmental gravitational field of the nearby universe, computed in a fully independent way.

3.2.3. Statistical Properties of the Posterior Parameters of the Galaxies

Figure 7 shows the distribution of the parameters from the MCMC simulations with Equation (5) for all 153 selected galaxies. The distribution of the distances is consistent with the SPARC reported values with an rms scatter of 0.02 dex (5%). This is smaller than typical measurement uncertainties of $\sim$14%. The posterior inclination angles are also consistent with the SPARC reported values with an rms scatter of 2°.1, smaller than typical measurement uncertainties of $\sim 4°$. The distributions of the mass-to-light ratios ($\Upsilon_{\rm disk}$ and $\Upsilon_{\rm bul}$) for the disk and the bulge are consistent with the estimates from infrared studies, i.e., $\Upsilon_{\rm disk} = 0.5\ M_\odot/L_\odot$ and $\Upsilon_{\rm bul} = 0.7\ M_\odot/L_\odot$, with an rms scatter of 0.14 dex. If anything $\Upsilon_{\rm bul}$ might be 0.6, a little smaller than 0.7. Finally, the distribution of $\Upsilon_{\rm gas}$ is in excellent agreement with X^{-1} from Equation (4), giving a mean value of 1.38 ± 0.04, which is intermediate between a metal-poor dwarf galaxy with $X^{-1} = 1.34$ and a metal-rich giant spiral with $X^{-1} = 1.42$.

3.2.4. Analysis of Possible Systematic Effects

One may wonder whether the systematic deviations from Equation (1) are due to some systematic uncertainties. There are three main observational effects that may systematically affect the low-acceleration portion of the RAR: galaxy distances, the thickness of the gas disk, and possible variations of $M_\star/L$ in the stellar disk with radius. To mitigate the first two uncertainties, the left panel of Figure 8 considers data points from galaxies with accurate distances based on the tip magnitude of the red giant

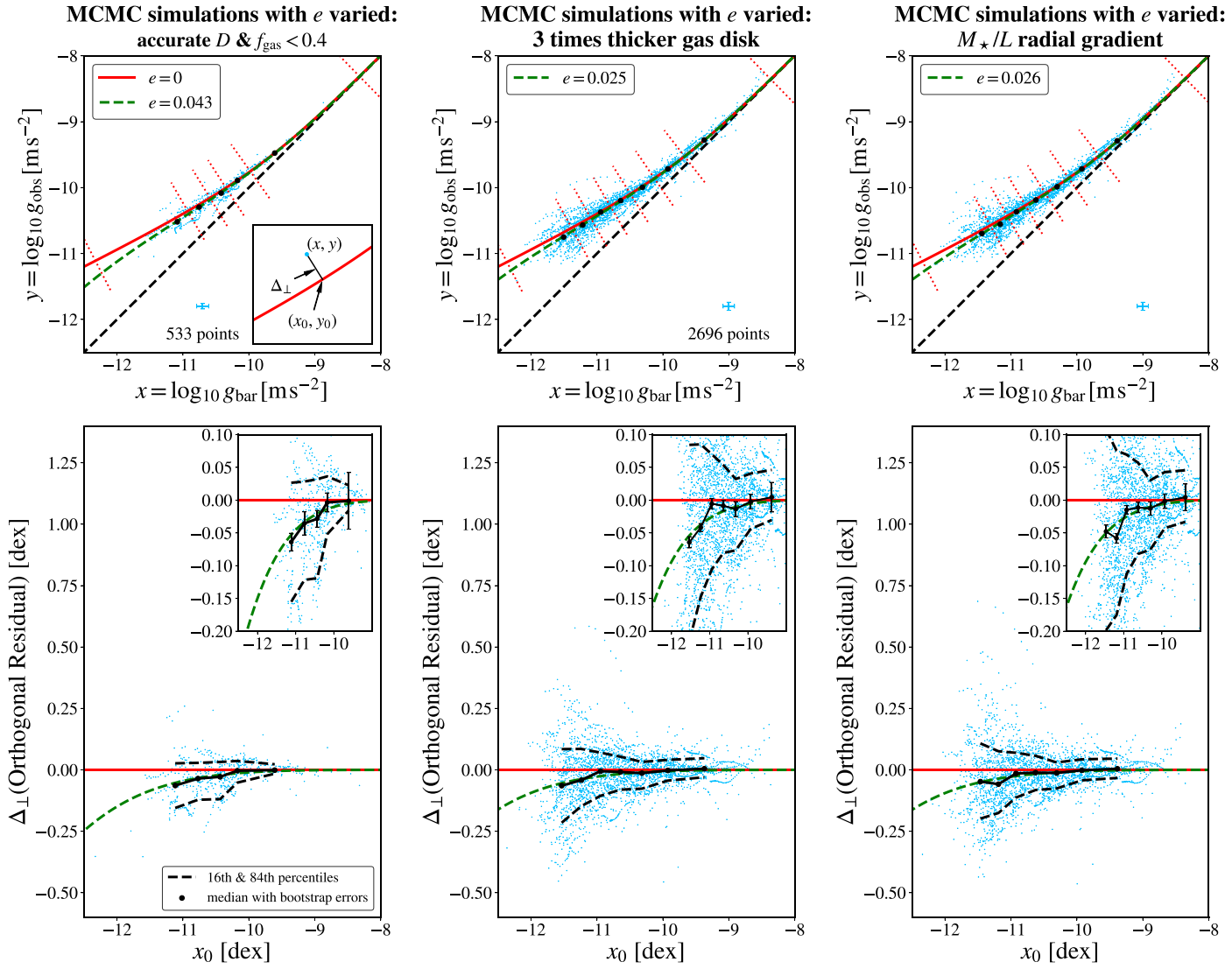

Figure 8. Testing systematic uncertainties in the EFE detection. This figure has the same format as Figure 3. The left panels show a subset of data points with subdominant gas contribution $f_{\rm gas} < 0.4$ and accurate distance measurements. The middle panels show the MCMC results assuming 3× thicker gas disks for all galaxies. The right panels show the MCMC results assuming a radial $M_\star/L$ gradient in the stellar disks of all galaxies. Our conclusions on the EFE detection hold in all cases.

branch, Cepheids, or supernovae (Lelli et al. 2016), as well as low gas contributions ($f_{\rm gas} = M_{\rm gas}/M_{\rm bar} < 0.4$). Compared with Figure 3, it is clear that the scatter is smaller and the median trend is consistent with the full data set.

The thickness of the gas disk is a concern because the EFE is detected in the galaxy outskirts, where the gas contribution becomes nonnegligible or even dominating in some cases. Recent studies (Bacchini et al. 2019) suggest that gas disks may become thicker at large radii: this would systematically decrease $V_{\rm gas}$, hence $g_{\rm bar}$, moving points to the left of the RAR. Therefore, we repeat the MCMC fits considering gas disks that are 3 times thicker than assumed in the SPARC database. This is a very extreme scenario because not all galaxies will have such thick gas disks. Our goal is simply to provide an upper bound on the possible impact of this effect. Figure 8 (middle panel) shows that there is still a significant systematic deviation from Equation (1) even when we consider very thick gas disks.

Negative gradients of $M_\star/L$ with R could also systematically decrease $V_{\rm disk}$, hence $g_{\rm bar}$, moving points to the left of the RAR. While we are treating the bulge separately in the most massive spirals (Sa to Sb), the stellar disk may potentially display a radial variation of its stellar populations. At 3.6 μm these variations have a relatively weak effect (Schombert et al. 2019), but we nevertheless repeat the MCMC fits considering a linear decrease in $\Upsilon_{\rm disk}$ by a factor of 2 from the center to the outermost observed radius. Again, this is an extreme scenario since most stellar disk are likely not showing such strong radial gradients in $\Upsilon_{\rm disk}$. Figure 8 (right panel) shows that there is still a significant systematic deviation from Equation (1).

3.3. Comparison with Previous Results

Only a few attempts have been made so far to detect the EFE from the RCs of galaxies (Wu & Kroupa 2015; Haghi et al. 2016). In particular, Haghi et al. (2016) considered the RCs of 18 galaxies taken from the literature available at that time. These galaxies are known to have relatively nearby massive neighbors. Eleven of them are also included in our sample of 153 galaxies studied here. They are DDO 154, IC 2574, NGC 2998, NGC 3198, NGC 3521, NGC 3769, NGC 4100, NGC 4183, NGC 5033, NGC 5055, and NGC 5371.

Haghi et al. (2016) obtained values of e ranging from about 0.1 to 0.6 with a median of ∼0.3 and a typical uncertainty of ∼0.1 for these 11 galaxies. Their values are systematically higher than our values ranging from about −0.1 to 0.3 with a median of ∼0.075 and a typical uncertainty of ∼0.04. This is primarily due to the fact that the disk models of Haghi et al. (2016) are based on a baryonic mass profile that declines more slowly than observed at large radii, requiring a larger EFE in the MOND context (a deficit of DM in the ΛCDM context).

There have also been indications of the EFE in pressure-supported galaxies (McGaugh & Milgrom 2013a, 2013b; Famaey et al. 2018; Kroupa et al. 2018). Pressure-supported galaxies are analyzed through their observed line-of-sight velocity dispersions. Because their stellar orbits are complex and not observed directly, a robust kinematic analysis to infer the EFE is challenging. However, McGaugh & Milgrom (2013a, 2013b) have found that the observed velocity dispersions of the dwarf galaxies of the Andromeda galaxy are consistent with a MOND theory with EFE. More recently, galaxies that appeared to have too low observed velocity dispersions and thus lack dark matter in the ΛCDM context (van Dokkum et al. 2018, 2019) may well be explained by the MOND EFE (Famaey et al. 2018; Kroupa et al. 2018; Haghi et al. 2019; Müller et al. 2019).

4. Discussion

Galaxies of similar properties but subjected to different external gravitational fields show noticeably different rotation-curve behaviors at large radii (i.e., at very low accelerations). Two galaxies in the strongest environmental fields show declining RCs in the outer parts, while two similar galaxies in the weakest environmental fields have flat RCs. The connection between internal dynamics and large-scale environment is corroborated by a statistical analysis of the entire SPARC sample. At accelerations 10 times lower than $g_\dagger$, the RAR is not fully described by a simple function of $g_{\rm bar}/g_\dagger$ (Equation (1)) but requires an EFE-incorporated generalized function with an additional free parameter e (Equation (6)). Moreover, rotation-curve fits with Equation (6) give a mean value of e that is indistinguishable from the mean environmental gravitational field at the location of SPARC galaxies, computed in a fully independent fashion from the average distribution of mass in the nearby universe. These results are summarized in Figures 3 and 5. Note that these results of fitting Equation (6) to RCs are fully *empirical*, independent of any theoretical interpretation.

Can these results be explained in the standard ΛCDM framework? For the two golden massive galaxies subjected to strong large-scale gravitational field $g_{\rm env}$, declining RCs are observed over a radial range of about 30–50 kpc, which are less than ∼15% of the virial radius of the DM halo. Clearly, this is not the decline that should occur in the outer parts of ΛCDM halos, where the density profile decreases as r^{-3}, since we are probing the inner parts of the halo where the density profile goes approximately as r^{-2}, leading to flat RCs.

Thus, the only remaining option is represented by tidal forces. We calculated the expected tidal radii in ΛCDM using the formalism of King (1962), taking the source of the tidal field to be the nearest 2M++ galaxy to the SPARC galaxy in question. We assume the source and test galaxies to have Navarro–Frenk–White (Navarro et al. 1997) halos following the $M_\star$–$M_{\rm vir}$ relation of Kravtsov et al. (2018) and the $M_{\rm vir}$−concentration relation of Diemer & Kravtsov (2015). We find the tidal radii to be much larger than the last measured points of the RCs, so the galaxies themselves are effectively shielded against large-scale tides.

The agreement between the MOND fitting parameter e (Equation (6)) and the environmental gravitational field $e_{\rm env}$ is an unpredicted result from the ΛCDM point of view. In principle, the baryon plus DM combination can combine to produce a declining rotation curve within tens of kiloparsecs as found here (i.e., $e > 0$). For that matter, however, there is no a priori reason that the degree of declining must agree with the strength of the environmental gravitational field. There could have been an order-of-magnitude difference between e and $e_{\rm env}$. Yet, we are seeing an interesting coincidence between the two.

Moreover, a downward deviation in the RAR near a tenth of $g_\dagger$ is not predicted by current ΛCDM state-of-the-art simulations or semianalytical models (Di Cintio & Lelli 2016; Desmond 2017; Keller & Wadsley 2017; Navarro et al. 2017; Tenneti et al. 2018) with some predicting the opposite trend (Ludlow et al. 2017; Fattahi et al. 2018; Garaldi et al. 2019). To the best of our knowledge, there is no reported scenario in which the DM–baryon coupling in the outskirts of the disks depends on the external gravitational field from the large-scale galaxy environment in the manner found here.

The empirical evidence is fully consistent with the EFE predicted by MOND modified gravity (Bekenstein & Milgrom 1984). More generally, our results suggest a violation of the SEP in rotationally supported galaxies. While in GR the internal dynamics of a gravitationally bound system is not affected by a uniform external field, our analysis indicates that external fields *do* impact the internal dynamics. Our results are encouraging for modified gravity as an alternative (or modification) to the DM hypothesis and the standard ΛCDM cosmological model. They also highlight the path for future theoretical investigations of relativistic theories of gravity beyond GR (see, e.g., Skordis & Złośnik 2020), possibly leading to a new cosmological model.

5. Conclusions

In this paper we provide observational evidence for the existence of the EFE (or a phenomenon akin to it) predicted by MOND modified gravity (Bekenstein & Milgrom 1984). We use accurate rotation curves and mass models from the SPARC database (Lelli et al. 2016) and detect the EFE in three separate ways:

1. The EFE is individually detected in "golden" galaxies subjected to exceptionally strong external gravitational fields. The detection is highly significant (11σ in NGC 5055 and 8σ in NGC 5033) and the best-fit values of the external gravitational fields are fully consistent with the independent estimates from the large-scale distribution of mass at the galaxies' location. Conversely, the EFE is not detected in control galaxies residing in the weakest external gravitational fields, as expected.
2. The EFE is statistically detected at more than 4σ through a blind test using 153 SPARC galaxies. The mean value of the external gravitational field among the SPARC galaxies is again consistent with the independent estimate from the average distribution of mass in the nearby universe.
3. The EFE also manifests as a small ($\gtrsim$0.05 dex), downward deviation from the empirical RAR occurring around $0.1g_\dagger$. This behavior is not predicted by any of the existing galaxy formation models in ΛCDM that were

proposed to "naturally" reproduce the RAR. In contrast, this downward deviation *is* predicted by the MOND modified gravity at the right acceleration scale.

Our results suggest a breakdown of the SEP: the internal dynamics of a gravitational system in freefall *is* affected by a uniform external gravitational field. This sheds new light on the dark-matter problem and paves the way for relativistic theories of modified gravity in the weak-field regime of gravity $g \lesssim 10^{-10}$ m s^{-2}.

We thank the organizers of the conference Bonn-Gravity 2019 (Pavel Kroupa and Indranil Banik) where several of these issues were brought to light. We thank Andrey Kravtsov for providing a code to calculate tidal radii of ΛCDM halos. This work was supported by the National Research Foundation of Korea (NRF) grant funded by the Korea government (MSIT) (No. NRF-2019R1F1A1062477). H.D. is supported by St John's college, Oxford, and acknowledges financial support from ERC grant No. 693024 and the Beecroft Trust. The Work of S.S.M. is supported in part by NASA ADAP 80NSSC19k0570 and NSF PHY-1911909.

Appendix A
The Posterior PDFs of the Parameters: Golden and Normal Galaxies

We present the full posterior PDFs of the parameters for the two golden galaxies NGC 5033 and NGC 5055, which are found in the strongest external fields among the SPARC

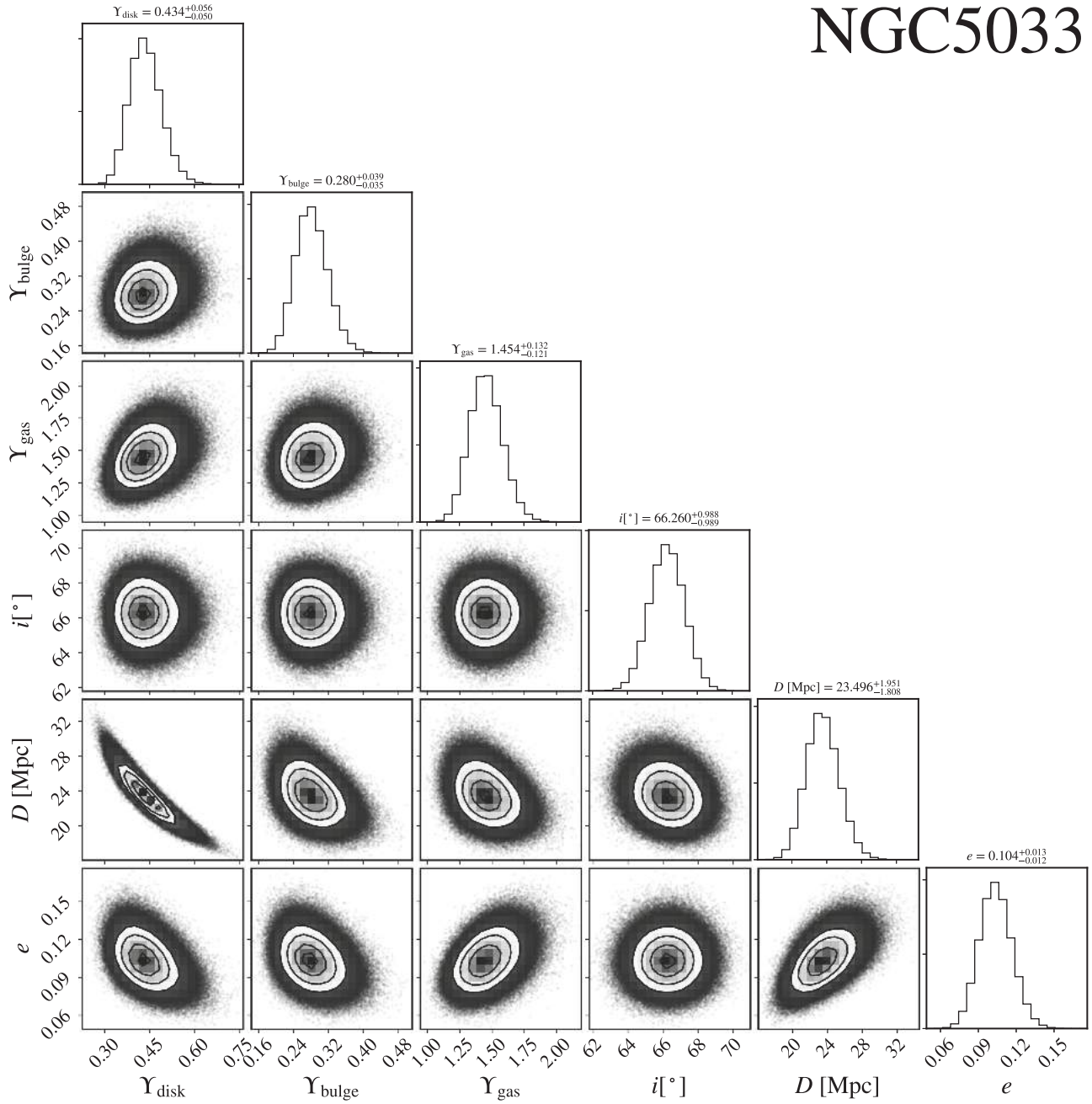

Figure 9. Parameter corner plot for NGC 5033. The posterior PDFs of the parameters for "golden galaxy" NGC 5033 produced from MCMC simulations using Equation (5).

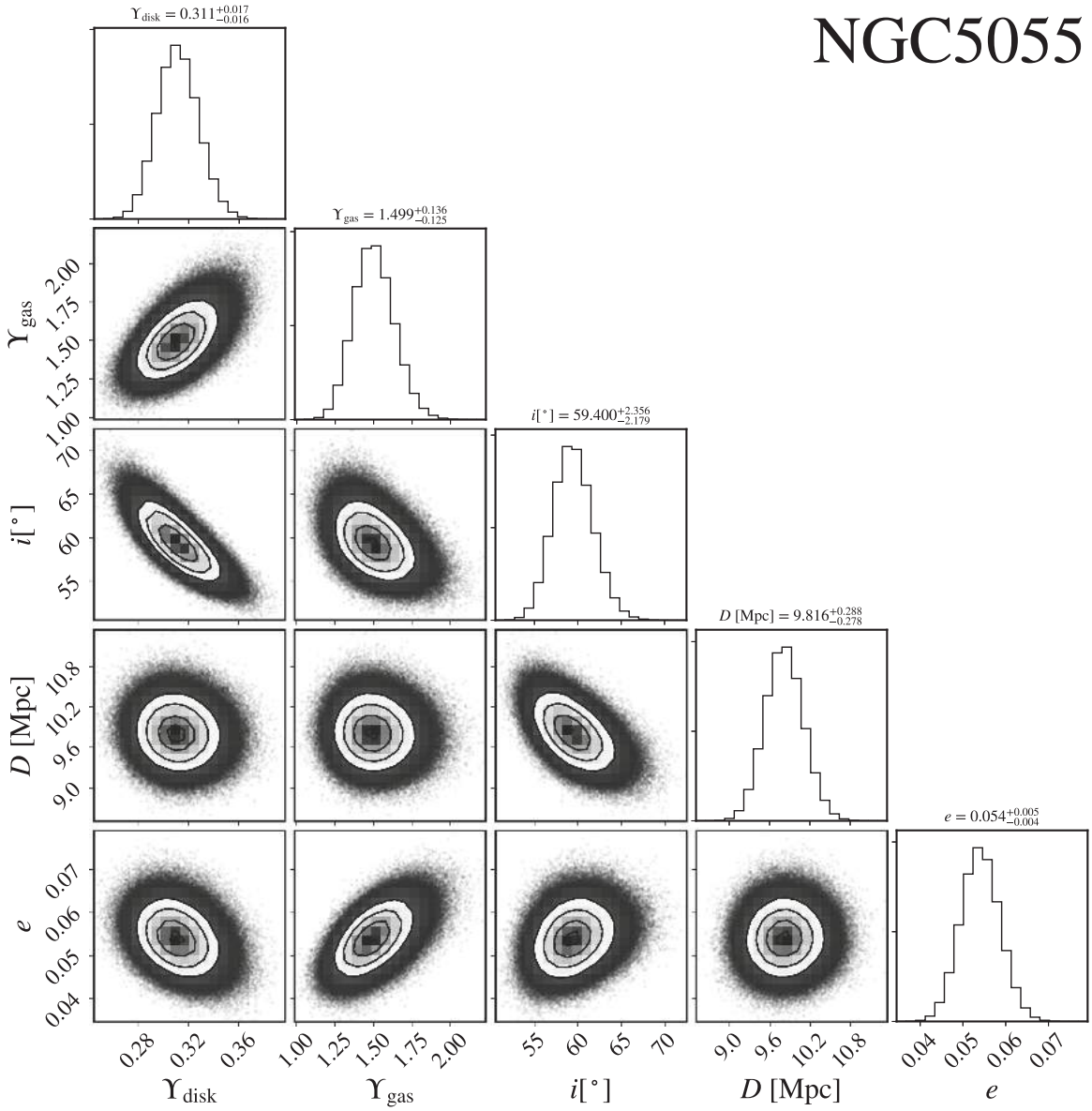

Figure 10. Parameter corner plot for NGC 5055. The posterior PDFs of the parameters for "golden galaxy" NGC 5055 produced from MCMC simulations using Equation (5).

galaxies. NGC 5033 (Figure 9) has a bulge component while NGC 5055 (Figure 10) does not. These are the cases in which e is well constrained.

We also present the two control galaxies NGC 1090 (Figure 11) and NGC 6674 (Figure 12) that are found in the weakest external fields among the SPARC galaxies. These galaxies have statistical uncertainties of $\sim$0.02 in e, which are lower than typical uncertainties of $\sim$0.04 across the whole sample. Thus, we show another two examples, NGC 2955 (Figure 13) and NGC 6195 (Figure 14), that have statistical uncertainties of $\sim$0.04 in e. Unlike the golden galaxies, e is hardly constrained in these normal galaxies.

The corner plots for all 153 galaxies can be found at http://astroweb.cwru.edu/SPARC/.

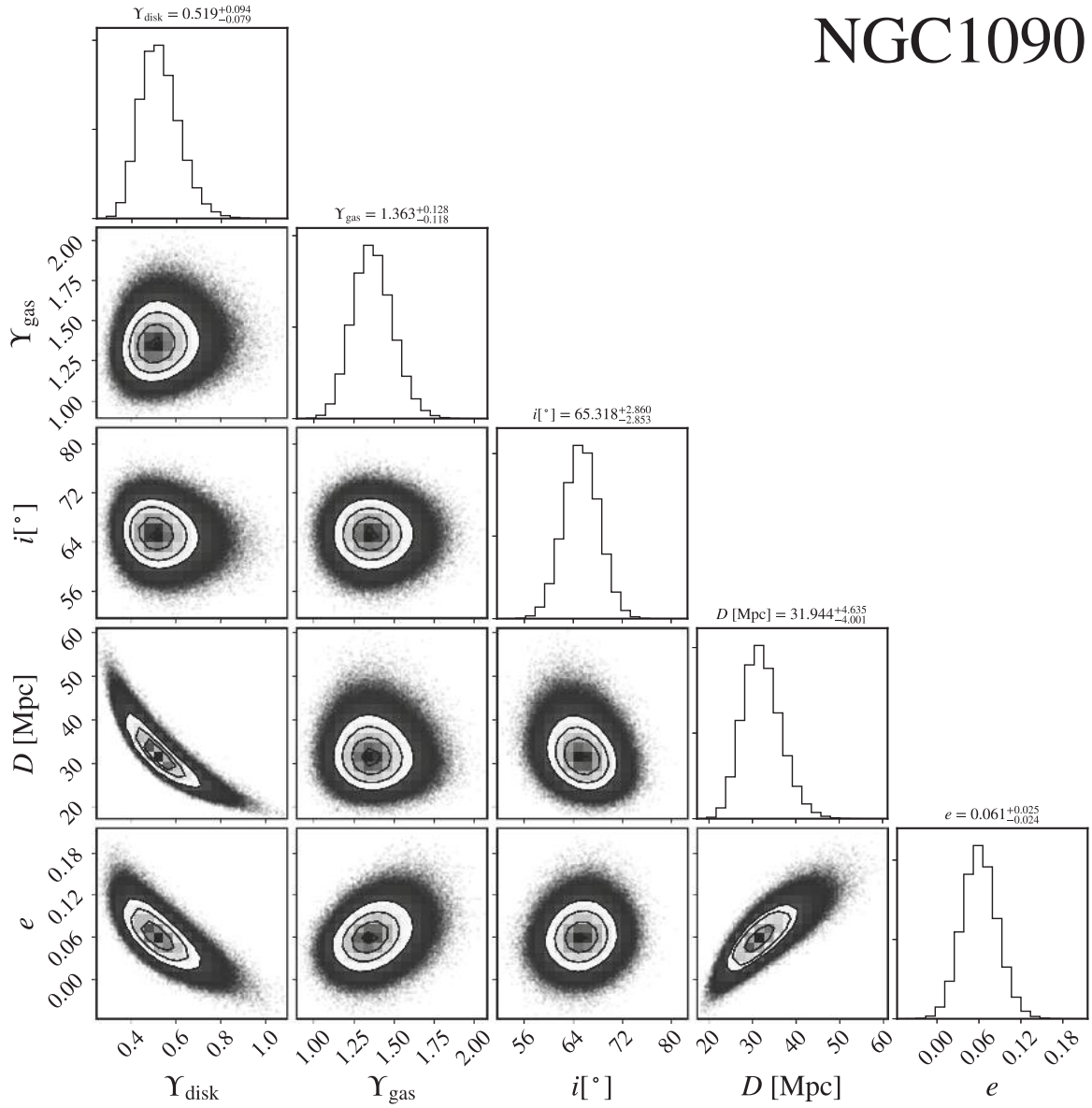

Figure 11. Parameter corner plot for NGC 1090. The posterior PDFs of the parameters for a control galaxy NGC 1090 produced from MCMC simulations using Equation (5).

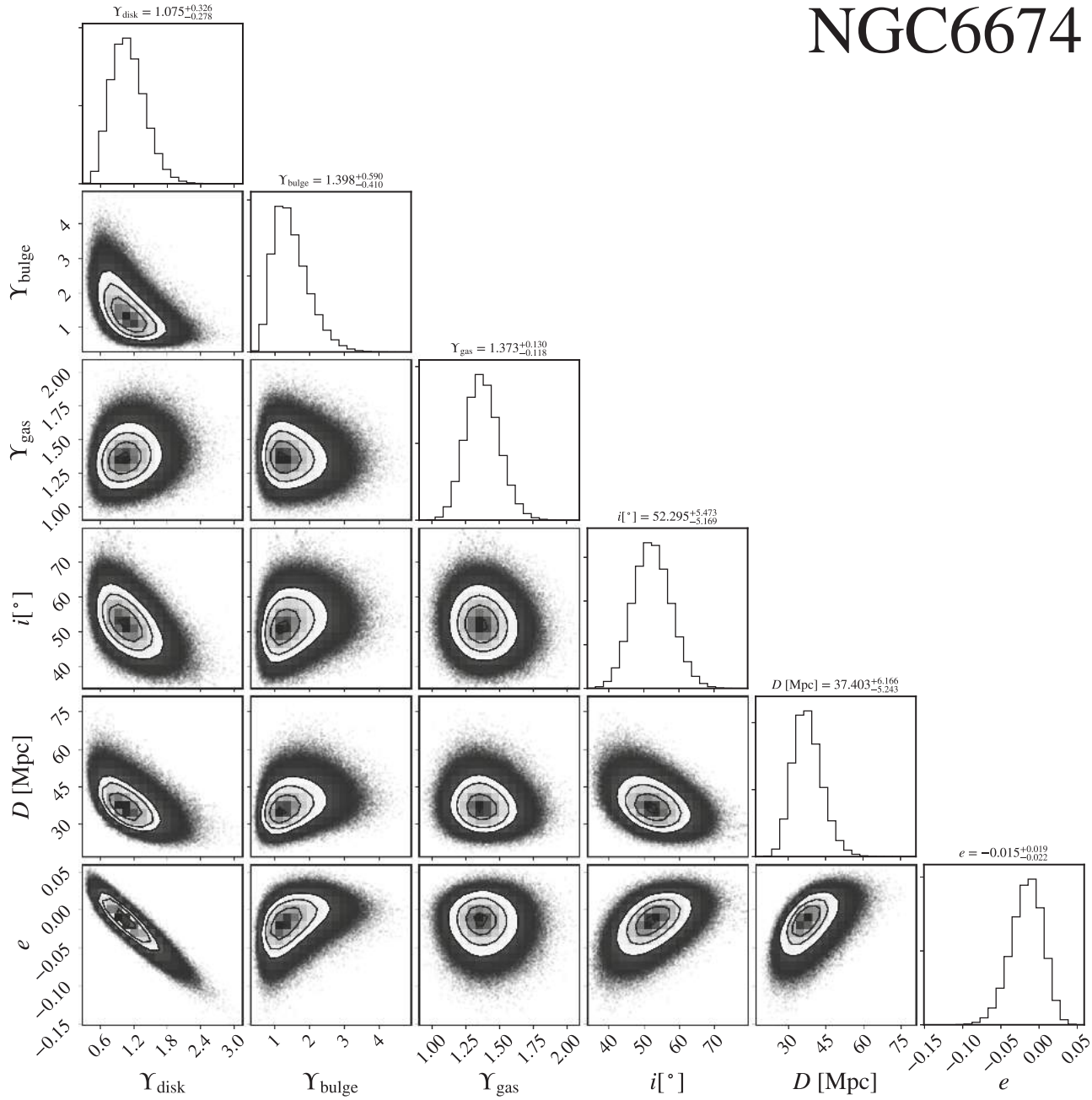

Figure 12. Parameter corner plot for NGC 6674. The posterior PDFs of the parameters for a control galaxy NGC 6674 produced from MCMC simulations using Equation (5).

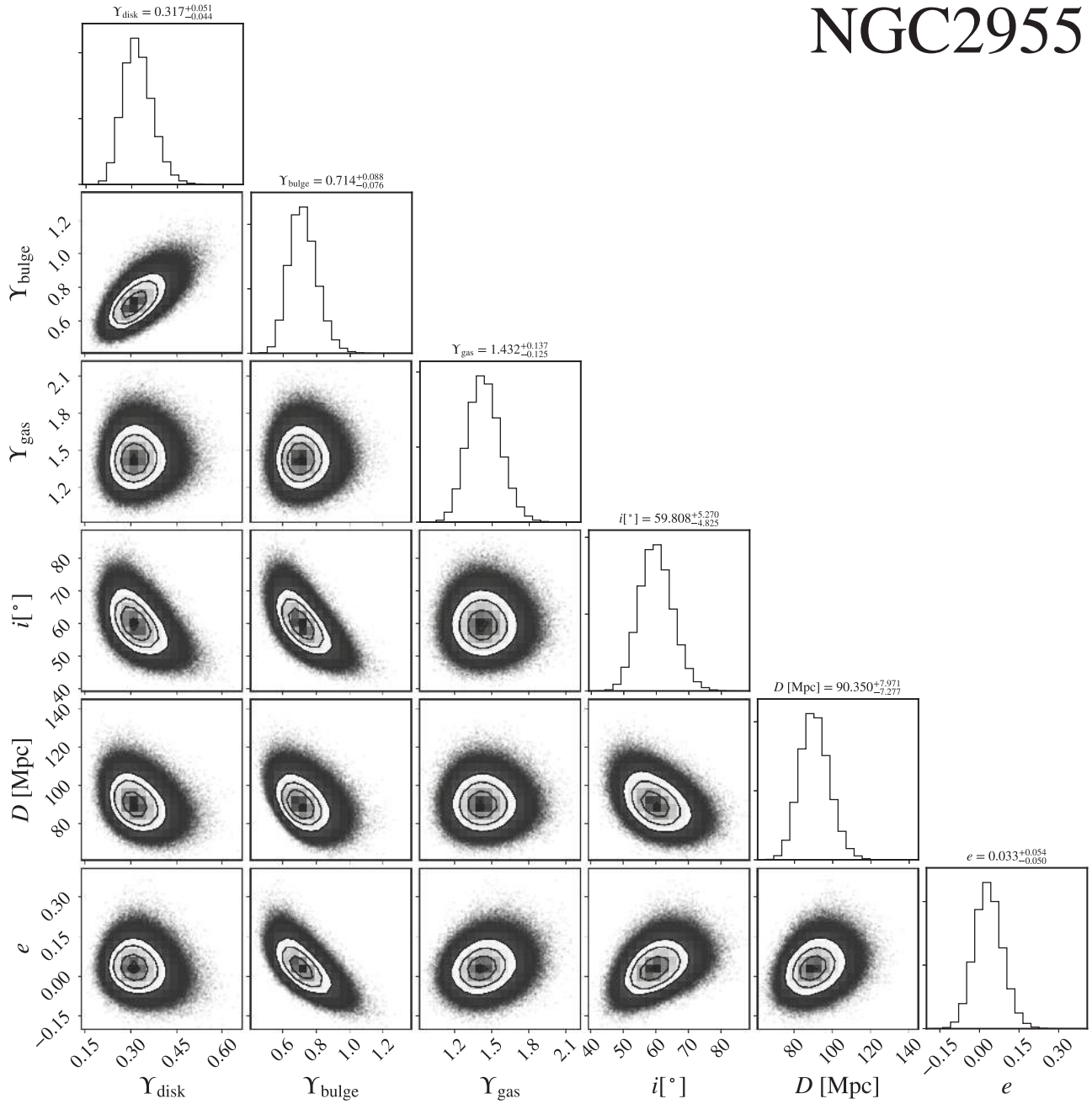

Figure 13. Parameter corner plot for NGC 2955. The posterior PDFs of the parameters for a normal galaxy NGC 2955 produced from MCMC simulations using Equation (5).

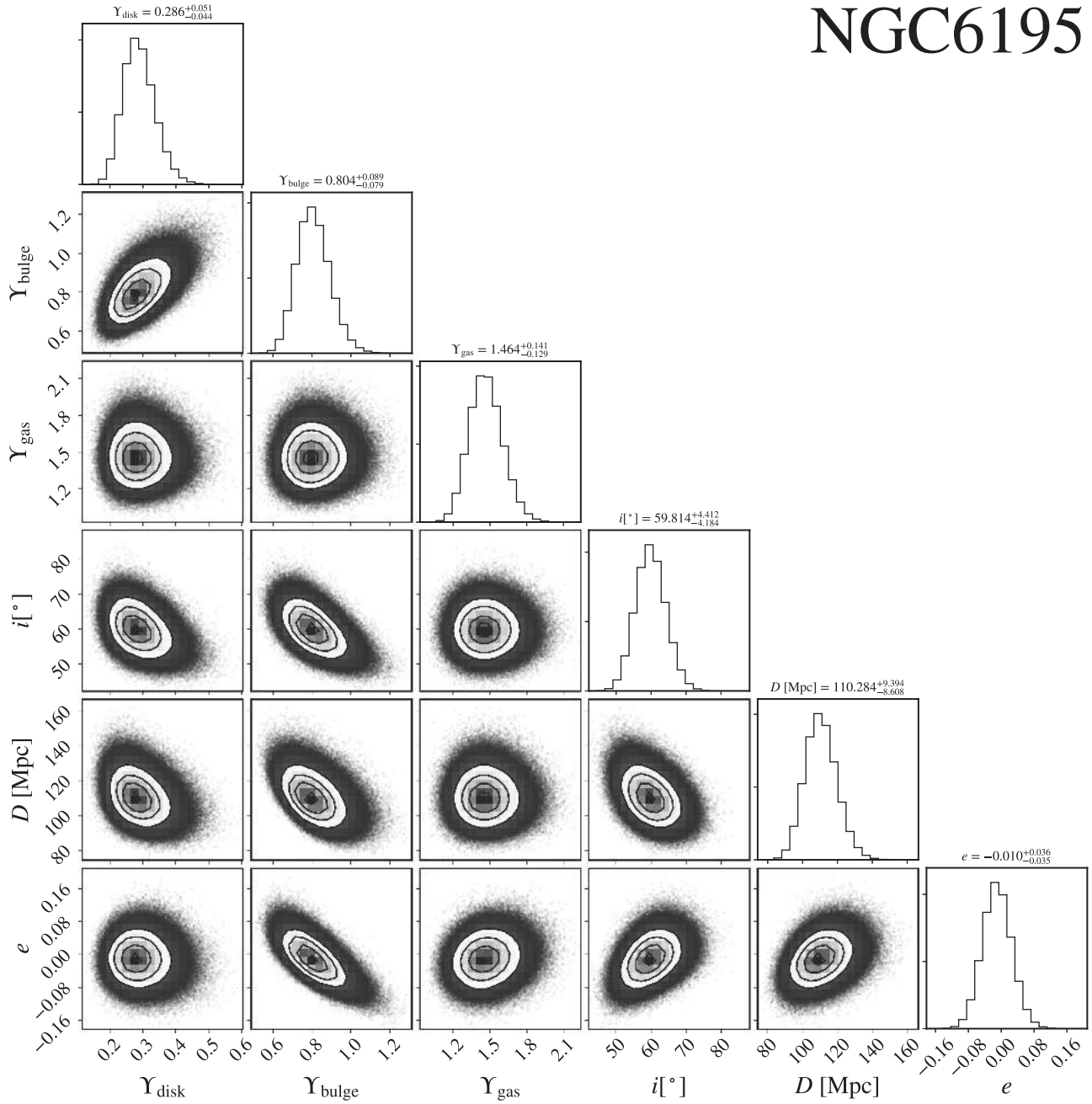

Figure 14. Parameter corner plot for NGC 6195. The posterior PDFs of the parameters for a normal galaxy NGC 6195 produced from MCMC simulations using Equation (5).

Appendix B
Fitted Values of the Parameters

The MCMC fitted values of the model parameters and the independent estimate of $e_{\rm env}$ from the environment can be found in Table 2 for the 153 SPARC galaxies. The values are also available in a machine format at http://astroweb.cwru.edu/SPARC/. The MCMC value and its uncertainty come from the 50th percentile and the 15.9 and 84.1 percentiles of the posterior PDF. Note that the values of e are not meaningful for galaxies with $\langle x_0 \rangle \gtrsim -10$ because the EFE has little effect on the rotation velocities in the high acceleration range. See Section 3.2.

Table 2
Fitted Model Parameters

Galaxy	$\langle x_0 \rangle$	e	$e_{\rm env}$	D (Mpc)	i (°)	$\Upsilon_{\rm gas}$	$\Upsilon_{\rm disk}$	$\Upsilon_{\rm bulge}$
CamB	-11.736	$0.461^{+0.029}_{-0.054}$	$0.021^{+0.004}_{-0.003}$	$3.07^{+0.22}_{-0.21}$	$59.04^{+4.84}_{-4.63}$	$1.27^{+0.12}_{-0.11}$	$0.32^{+0.06}_{-0.05}$	⋯
D512-2	-11.423	$0.119^{+0.136}_{-0.088}$	$0.035^{+0.006}_{-0.005}$	$16.12^{+4.76}_{-3.74}$	$61.47^{+9.02}_{-8.94}$	$1.36^{+0.13}_{-0.12}$	$0.52^{+0.13}_{-0.11}$	⋯
D564-8	-11.987	$0.067^{+0.028}_{-0.027}$	$0.028^{+0.005}_{-0.004}$	$8.75^{+0.28}_{-0.27}$	$61.53^{+7.46}_{-7.60}$	$1.37^{+0.13}_{-0.12}$	$0.41^{+0.10}_{-0.08}$	⋯
D631-7	-11.410	$-0.085^{+0.016}_{-0.017}$	$0.023^{+0.004}_{-0.003}$	$7.48^{+0.17}_{-0.17}$	$38.76^{+2.35}_{-2.27}$	$1.12^{+0.10}_{-0.09}$	$0.26^{+0.05}_{-0.04}$	⋯
DDO 064	-11.080	$0.063^{+0.126}_{-0.084}$	$0.029^{+0.006}_{-0.005}$	$6.97^{+2.14}_{-1.55}$	$63.29^{+4.68}_{-4.65}$	$1.35^{+0.13}_{-0.12}$	$0.53^{+0.13}_{-0.10}$	⋯
DDO 154	-11.526	$0.008^{+0.008}_{-0.008}$	$0.030^{+0.006}_{-0.005}$	$3.86^{+0.17}_{-0.16}$	$61.88^{+2.65}_{-2.55}$	$1.43^{+0.12}_{-0.11}$	$0.20^{+0.03}_{-0.03}$	⋯
DDO 161	-11.281	$-0.044^{+0.010}_{-0.010}$	$0.031^{+0.011}_{-0.008}$	$3.37^{+0.40}_{-0.30}$	$73.91^{+7.96}_{-7.97}$	$1.37^{+0.13}_{-0.12}$	$0.33^{+0.07}_{-0.06}$	⋯
DDO 168	-10.931	$-0.188^{+0.043}_{-0.050}$	$0.028^{+0.005}_{-0.004}$	$4.05^{+0.20}_{-0.19}$	$35.82^{+3.72}_{-3.55}$	$1.24^{+0.12}_{-0.11}$	$0.44^{+0.11}_{-0.09}$	⋯
DDO 170	-11.461	$0.038^{+0.021}_{-0.018}$	$0.049^{+0.008}_{-0.007}$	$11.82^{+1.87}_{-1.51}$	$66.33^{+6.65}_{-6.40}$	$1.28^{+0.12}_{-0.11}$	$0.67^{+0.14}_{-0.12}$	⋯
ESO 079-G014	-10.517	$-0.028^{+0.058}_{-0.055}$	$0.014^{+0.002}_{-0.002}$	$28.21^{+4.57}_{-3.91}$	$80.00^{+4.56}_{-4.66}$	$1.38^{+0.13}_{-0.12}$	$0.56^{+0.11}_{-0.09}$	⋯
ESO 116-G012	-10.715	$-0.062^{+0.041}_{-0.040}$	$0.016^{+0.003}_{-0.003}$	$13.50^{+2.46}_{-2.03}$	$74.69^{+2.92}_{-2.92}$	$1.39^{+0.14}_{-0.12}$	$0.45^{+0.10}_{-0.08}$	⋯
ESO 444-G084	-11.071	$-0.090^{+0.027}_{-0.031}$	$0.031^{+0.009}_{-0.007}$	$4.68^{+0.45}_{-0.41}$	$33.13^{+3.03}_{-2.89}$	$1.34^{+0.13}_{-0.12}$	$0.47^{+0.12}_{-0.09}$	⋯
ESO 563-G021	-10.059	$-0.031^{+0.032}_{-0.033}$	$0.034^{+0.018}_{-0.012}$	$66.48^{+8.08}_{-7.21}$	$83.63^{+2.77}_{-2.81}$	$1.45^{+0.14}_{-0.13}$	$0.69^{+0.10}_{-0.09}$	⋯
F565-V2	-11.436	$-0.013^{+0.047}_{-0.047}$	$0.012^{+0.003}_{-0.003}$	$52.32^{+10.73}_{-8.90}$	$65.91^{+8.87}_{-8.91}$	$1.36^{+0.13}_{-0.12}$	$0.50^{+0.13}_{-0.10}$	⋯
F568-3	-11.252	$0.268^{+0.117}_{-0.096}$	$0.008^{+0.002}_{-0.002}$	$84.28^{+8.09}_{-7.46}$	$61.93^{+6.95}_{-6.78}$	$1.42^{+0.13}_{-0.12}$	$0.47^{+0.08}_{-0.07}$	⋯
F568-V1	-10.954	$0.106^{+0.077}_{-0.060}$	$0.006^{+0.005}_{-0.003}$	$85.62^{+8.25}_{-7.51}$	$64.28^{+6.70}_{-6.37}$	$1.32^{+0.13}_{-0.11}$	$0.82^{+0.16}_{-0.14}$	⋯
F571-8	-10.730	$-0.349^{+0.038}_{-0.041}$	$0.005^{+0.003}_{-0.002}$	$27.74^{+3.96}_{-3.51}$	$82.84^{+4.35}_{-5.16}$	$1.38^{+0.13}_{-0.12}$	$0.23^{+0.04}_{-0.04}$	⋯
F571-V1	-11.479	$0.229^{+0.146}_{-0.121}$	$0.009^{+0.002}_{-0.002}$	$80.12^{+7.86}_{-7.16}$	$44.11^{+7.34}_{-7.86}$	$1.38^{+0.13}_{-0.12}$	$0.47^{+0.11}_{-0.09}$	⋯
F574-1	-11.066	$0.085^{+0.054}_{-0.045}$	$0.010^{+0.001}_{-0.001}$	$100.59^{+9.53}_{-8.66}$	$75.22^{+7.04}_{-7.10}$	$1.32^{+0.12}_{-0.11}$	$0.78^{+0.14}_{-0.12}$	⋯
F583-1	-11.337	$0.035^{+0.059}_{-0.052}$	$0.014^{+0.002}_{-0.002}$	$36.15^{+8.53}_{-6.89}$	$67.66^{+4.49}_{-4.48}$	$1.24^{+0.11}_{-0.10}$	$0.96^{+0.16}_{-0.14}$	⋯
F583-4	-11.358	$0.090^{+0.092}_{-0.067}$	$0.012^{+0.002}_{-0.002}$	$52.94^{+10.66}_{-8.80}$	$64.76^{+8.35}_{-8.19}$	$1.37^{+0.13}_{-0.12}$	$0.49^{+0.12}_{-0.10}$	⋯
IC 2574	-11.722	$0.075^{+0.017}_{-0.015}$	$0.016^{+0.001}_{-0.001}$	$4.01^{+0.19}_{-0.18}$	$81.45^{+4.57}_{-4.84}$	$1.66^{+0.13}_{-0.12}$	$0.20^{+0.03}_{-0.03}$	⋯
IC 4202	-9.998	$0.187^{+0.064}_{-0.056}$	$0.026^{+0.024}_{-0.012}$	$99.16^{+7.71}_{-7.23}$	$89.33^{+0.47}_{-0.73}$	$1.26^{+0.11}_{-0.11}$	$0.90^{+0.09}_{-0.09}$	$0.44^{+0.04}_{-0.04}$
KK98-251	-11.423	$0.293^{+0.125}_{-0.111}$	$0.027^{+0.002}_{-0.002}$	$7.21^{+1.42}_{-1.39}$	$62.71^{+4.54}_{-4.50}$	$1.37^{+0.13}_{-0.12}$	$0.47^{+0.12}_{-0.09}$	⋯
NGC 0024	-10.096	$-0.004^{+0.017}_{-0.016}$	$0.027^{+0.005}_{-0.004}$	$7.48^{+0.35}_{-0.34}$	$67.27^{+2.71}_{-2.68}$	$1.34^{+0.13}_{-0.12}$	$0.99^{+0.11}_{-0.10}$	⋯
NGC 0055	-11.110	$0.052^{+0.023}_{-0.020}$	$0.029^{+0.004}_{-0.003}$	$1.94^{+0.09}_{-0.09}$	$75.23^{+3.14}_{-3.11}$	$1.33^{+0.12}_{-0.11}$	$0.21^{+0.04}_{-0.03}$	⋯
NGC 0100	-10.989	$-0.099^{+0.035}_{-0.038}$	$0.016^{+0.002}_{-0.001}$	$9.72^{+1.89}_{-1.56}$	$88.80^{+0.74}_{-0.91}$	$1.39^{+0.14}_{-0.12}$	$0.39^{+0.09}_{-0.07}$	⋯
NGC 0247	-10.915	$0.202^{+0.069}_{-0.055}$	$0.015^{+0.003}_{-0.003}$	$3.76^{+0.19}_{-0.18}$	$75.59^{+2.83}_{-2.83}$	$1.29^{+0.12}_{-0.11}$	$1.03^{+0.12}_{-0.11}$	⋯
NGC 0289	-11.225	$0.125^{+0.036}_{-0.029}$	$0.006^{+0.001}_{-0.001}$	$19.93^{+3.17}_{-2.65}$	$54.37^{+4.10}_{-3.99}$	$1.43^{+0.13}_{-0.12}$	$0.44^{+0.07}_{-0.06}$	⋯
NGC 0300	-11.083	$-0.009^{+0.026}_{-0.025}$	$0.026^{+0.006}_{-0.005}$	$2.03^{+0.10}_{-0.09}$	$47.31^{+5.37}_{-4.58}$	$1.34^{+0.13}_{-0.12}$	$0.40^{+0.08}_{-0.06}$	⋯
NGC 0801	-10.204	$0.190^{+0.029}_{-0.027}$	$0.035^{+0.010}_{-0.008}$	$68.49^{+6.51}_{-5.86}$	$79.93^{+1.00}_{-1.00}$	$1.44^{+0.14}_{-0.13}$	$0.60^{+0.07}_{-0.06}$	⋯
NGC 0891	-10.025	$-0.110^{+0.020}_{-0.019}$	$0.027^{+0.003}_{-0.003}$	$9.84^{+0.46}_{-0.44}$	$89.33^{+0.47}_{-0.73}$	$1.34^{+0.13}_{-0.11}$	$0.33^{+0.02}_{-0.02}$	$0.52^{+0.06}_{-0.06}$
NGC 1003	-11.250	$-0.054^{+0.008}_{-0.008}$	$0.017^{+0.003}_{-0.003}$	$6.54^{+0.65}_{-0.58}$	$70.18^{+4.54}_{-4.48}$	$1.22^{+0.11}_{-0.10}$	$0.77^{+0.11}_{-0.10}$	⋯
NGC 1090	-10.626	$0.061^{+0.025}_{-0.024}$	$0.023^{+0.005}_{-0.004}$	$31.94^{+4.66}_{-4.02}$	$65.32^{+2.88}_{-2.87}$	$1.36^{+0.13}_{-0.12}$	$0.52^{+0.09}_{-0.08}$	⋯
NGC 2403	-10.435	$-0.019^{+0.005}_{-0.005}$	$0.014^{+0.002}_{-0.002}$	$3.59^{+0.13}_{-0.13}$	$72.06^{+2.26}_{-2.21}$	$0.76^{+0.06}_{-0.05}$	$0.39^{+0.02}_{-0.02}$	⋯
NGC 2683	-10.612	$0.091^{+0.031}_{-0.028}$	$0.023^{+0.004}_{-0.003}$	$9.88^{+0.47}_{-0.45}$	$81.01^{+4.37}_{-4.53}$	$1.41^{+0.14}_{-0.12}$	$0.56^{+0.05}_{-0.05}$	$0.69^{+0.17}_{-0.14}$
NGC 2841	-9.797	$-0.027^{+0.012}_{-0.013}$	$0.014^{+0.002}_{-0.002}$	$14.03^{+0.98}_{-0.91}$	$82.99^{+4.43}_{-5.41}$	$1.31^{+0.12}_{-0.11}$	$0.91^{+0.10}_{-0.09}$	$0.96^{+0.08}_{-0.07}$
NGC 2903	-10.616	$0.040^{+0.008}_{-0.008}$	$0.022^{+0.005}_{-0.004}$	$12.47^{+0.97}_{-0.89}$	$69.15^{+2.76}_{-2.75}$	$1.26^{+0.11}_{-0.10}$	$0.18^{+0.02}_{-0.02}$	⋯
NGC 2915	-11.531	$-0.052^{+0.012}_{-0.013}$	$0.028^{+0.010}_{-0.007}$	$4.12^{+0.20}_{-0.19}$	$62.30^{+3.41}_{-3.37}$	$1.35^{+0.13}_{-0.12}$	$0.58^{+0.11}_{-0.09}$	⋯
NGC 2955	-9.783	$0.033^{+0.054}_{-0.051}$	$0.017^{+0.002}_{-0.002}$	$90.35^{+8.02}_{-7.31}$	$59.81^{+5.30}_{-4.85}$	$1.43^{+0.14}_{-0.13}$	$0.32^{+0.05}_{-0.04}$	$0.71^{+0.09}_{-0.08}$
NGC 2976	-10.365	$0.387^{+0.080}_{-0.114}$	$0.017^{+0.002}_{-0.002}$	$3.62^{+0.17}_{-0.17}$	$76.32^{+6.27}_{-6.13}$	$1.44^{+0.13}_{-0.12}$	$0.44^{+0.05}_{-0.05}$	⋯
NGC 2998	-10.488	$0.110^{+0.033}_{-0.030}$	$0.005^{+0.002}_{-0.001}$	$70.00^{+8.65}_{-7.59}$	$58.69^{+1.94}_{-1.94}$	$1.45^{+0.14}_{-0.13}$	$0.54^{+0.09}_{-0.07}$	⋯
NGC 3109	-11.513	$0.012^{+0.010}_{-0.010}$	$0.021^{+0.006}_{-0.004}$	$1.40^{+0.07}_{-0.06}$	$76.86^{+3.91}_{-3.81}$	$1.68^{+0.14}_{-0.13}$	$0.24^{+0.05}_{-0.04}$	⋯
NGC 3198	-10.613	$0.057^{+0.013}_{-0.012}$	$0.026^{+0.005}_{-0.004}$	$15.28^{+1.17}_{-1.08}$	$75.62^{+2.72}_{-2.69}$	$1.36^{+0.13}_{-0.12}$	$0.43^{+0.04}_{-0.04}$	⋯
NGC 3521	-9.407	$-0.106^{+0.055}_{-0.057}$	$0.025^{+0.004}_{-0.004}$	$6.65^{+1.12}_{-0.96}$	$78.31^{+4.34}_{-4.35}$	$1.42^{+0.14}_{-0.13}$	$0.56^{+0.10}_{-0.09}$	⋯
NGC 3726	-10.485	$-0.001^{+0.032}_{-0.030}$	$0.031^{+0.005}_{-0.004}$	$14.36^{+1.54}_{-1.39}$	$52.20^{+1.96}_{-1.95}$	$1.34^{+0.13}_{-0.12}$	$0.44^{+0.07}_{-0.06}$	⋯
NGC 3741	-11.765	$-0.015^{+0.009}_{-0.009}$	$0.027^{+0.003}_{-0.003}$	$3.10^{+0.16}_{-0.15}$	$69.55^{+3.93}_{-3.86}$	$1.35^{+0.13}_{-0.12}$	$0.34^{+0.06}_{-0.06}$	⋯
NGC 3769	-10.927	$0.022^{+0.019}_{-0.018}$	$0.026^{+0.004}_{-0.004}$	$17.36^{+1.75}_{-1.59}$	$70.20^{+1.97}_{-1.97}$	$1.41^{+0.14}_{-0.12}$	$0.38^{+0.07}_{-0.06}$	⋯
NGC 3877	-10.082	$0.253^{+0.158}_{-0.163}$	$0.026^{+0.008}_{-0.006}$	$17.39^{+2.01}_{-1.81}$	$76.04^{+1.00}_{-1.00}$	$1.39^{+0.13}_{-0.12}$	$0.50^{+0.08}_{-0.07}$	⋯
NGC 3893	-10.297	$-0.029^{+0.047}_{-0.046}$	$0.020^{+0.007}_{-0.005}$	$18.33^{+2.07}_{-1.86}$	$49.72^{+1.91}_{-1.91}$	$1.41^{+0.14}_{-0.12}$	$0.45^{+0.07}_{-0.06}$	⋯
NGC 3917	-10.601	$0.121^{+0.067}_{-0.055}$	$0.027^{+0.005}_{-0.004}$	$19.41^{+2.32}_{-2.05}$	$79.34^{+1.97}_{-1.96}$	$1.39^{+0.13}_{-0.12}$	$0.61^{+0.10}_{-0.08}$	⋯
NGC 3949	-9.859	$0.005^{+0.228}_{-0.168}$	$0.015^{+0.009}_{-0.006}$	$17.03^{+2.08}_{-1.86}$	$55.03^{+1.97}_{-1.97}$	$1.40^{+0.13}_{-0.12}$	$0.43^{+0.07}_{-0.06}$	⋯
NGC 3953	-9.950	$0.393^{+0.077}_{-0.120}$	$0.025^{+0.006}_{-0.005}$	$18.62^{+2.15}_{-1.93}$	$62.11^{+0.99}_{-0.99}$	$1.41^{+0.14}_{-0.12}$	$0.59^{+0.08}_{-0.07}$	⋯
NGC 3972	-10.494	$-0.087^{+0.072}_{-0.063}$	$0.035^{+0.006}_{-0.005}$	$17.15^{+2.18}_{-1.93}$	$77.02^{+1.00}_{-1.00}$	$1.38^{+0.13}_{-0.12}$	$0.46^{+0.09}_{-0.08}$	⋯
NGC 3992	-10.447	$0.101^{+0.034}_{-0.031}$	$0.029^{+0.007}_{-0.005}$	$24.46^{+2.10}_{-1.93}$	$56.76^{+1.93}_{-1.92}$	$1.42^{+0.14}_{-0.12}$	$0.68^{+0.09}_{-0.08}$	⋯
NGC 4010	-10.623	$-0.053^{+0.050}_{-0.047}$	$0.025^{+0.006}_{-0.005}$	$16.33^{+2.03}_{-1.80}$	$88.80^{+0.75}_{-0.91}$	$1.41^{+0.14}_{-0.12}$	$0.36^{+0.07}_{-0.06}$	⋯
NGC 4013	-10.686	$-0.046^{+0.014}_{-0.015}$	$0.027^{+0.005}_{-0.004}$	$14.40^{+1.34}_{-1.24}$	$88.80^{+0.75}_{-0.91}$	$1.38^{+0.13}_{-0.12}$	$0.48^{+0.08}_{-0.07}$	$0.82^{+0.20}_{-0.16}$
NGC 4051	-10.191	$0.338^{+0.113}_{-0.155}$	$0.023^{+0.007}_{-0.005}$	$17.13^{+2.04}_{-1.83}$	$49.18^{+2.82}_{-2.78}$	$1.39^{+0.13}_{-0.12}$	$0.48^{+0.08}_{-0.07}$	⋯

Table 2
(Continued)

Galaxy	$\langle x_0 \rangle$	e	$e_{\rm env}$	D (Mpc)	i (°)	$\Upsilon_{\rm gas}$	$\Upsilon_{\rm disk}$	$\Upsilon_{\rm bulge}$
NGC 4068	-11.173	$0.344^{+0.103}_{-0.117}$	$0.027^{+0.007}_{-0.006}$	$4.36^{+0.22}_{-0.21}$	$47.34^{+4.47}_{-4.59}$	$1.38^{+0.13}_{-0.12}$	$0.43^{+0.09}_{-0.08}$	⋯
NGC 4085	-10.142	$-0.146^{+0.106}_{-0.086}$	$0.024^{+0.004}_{-0.003}$	$15.26^{+1.90}_{-1.69}$	$81.88^{+2.01}_{-2.02}$	$1.39^{+0.13}_{-0.12}$	$0.33^{+0.06}_{-0.05}$	⋯
NGC 4088	-10.303	$0.044^{+0.053}_{-0.048}$	$0.031^{+0.005}_{-0.004}$	$14.87^{+1.68}_{-1.51}$	$68.71^{+2.00}_{-2.00}$	$1.40^{+0.13}_{-0.12}$	$0.35^{+0.05}_{-0.05}$	⋯
NGC 4100	-10.442	$0.092^{+0.028}_{-0.027}$	$0.023^{+0.005}_{-0.004}$	$19.54^{+2.14}_{-1.92}$	$73.69^{+1.95}_{-1.95}$	$1.40^{+0.13}_{-0.12}$	$0.57^{+0.08}_{-0.07}$	⋯
NGC 4138	-10.020	$0.124^{+0.104}_{-0.080}$	$0.041^{+0.012}_{-0.009}$	$18.77^{+2.12}_{-1.90}$	$54.37^{+2.79}_{-2.76}$	$1.40^{+0.14}_{-0.12}$	$0.56^{+0.11}_{-0.09}$	$0.68^{+0.17}_{-0.14}$
NGC 4157	-10.510	$-0.016^{+0.031}_{-0.030}$	$0.039^{+0.008}_{-0.007}$	$15.23^{+1.61}_{-1.46}$	$81.93^{+2.98}_{-3.00}$	$1.40^{+0.13}_{-0.12}$	$0.42^{+0.06}_{-0.06}$	$0.65^{+0.16}_{-0.13}$
NGC 4183	-10.877	$0.115^{+0.039}_{-0.033}$	$0.025^{+0.005}_{-0.004}$	$18.22^{+2.04}_{-1.80}$	$82.23^{+1.97}_{-1.97}$	$1.33^{+0.13}_{-0.12}$	$0.69^{+0.11}_{-0.09}$	⋯
NGC 4217	-10.173	$-0.135^{+0.039}_{-0.039}$	$0.027^{+0.006}_{-0.005}$	$15.51^{+1.53}_{-1.40}$	$85.95^{+1.90}_{-1.97}$	$1.41^{+0.14}_{-0.12}$	$0.87^{+0.18}_{-0.15}$	$0.23^{+0.03}_{-0.03}$
NGC 4559	-10.832	$0.029^{+0.040}_{-0.036}$	$0.031^{+0.006}_{-0.005}$	$7.46^{+1.26}_{-1.04}$	$67.19^{+0.99}_{-0.99}$	$1.38^{+0.13}_{-0.12}$	$0.46^{+0.09}_{-0.07}$	⋯
NGC 5005	-9.452	$-0.080^{+0.252}_{-0.170}$	$0.028^{+0.005}_{-0.004}$	$16.19^{+1.24}_{-1.16}$	$68.17^{+1.97}_{-1.96}$	$1.42^{+0.14}_{-0.12}$	$0.50^{+0.08}_{-0.08}$	$0.54^{+0.08}_{-0.07}$
NGC 5033	-10.737	$0.104^{+0.013}_{-0.012}$	$0.026^{+0.005}_{-0.004}$	$23.50^{+1.96}_{-1.82}$	$66.26^{+0.99}_{-0.99}$	$1.45^{+0.13}_{-0.12}$	$0.43^{+0.06}_{-0.05}$	$0.28^{+0.04}_{-0.04}$
NGC 5055	-10.536	$0.054^{+0.005}_{-0.004}$	$0.028^{+0.006}_{-0.005}$	$9.82^{+0.29}_{-0.28}$	$59.40^{+2.37}_{-2.19}$	$1.50^{+0.14}_{-0.13}$	$0.31^{+0.02}_{-0.02}$	⋯
NGC 5371	-9.751	$0.284^{+0.054}_{-0.053}$	$0.030^{+0.004}_{-0.003}$	$16.48^{+2.50}_{-2.16}$	$52.12^{+2.00}_{-2.00}$	$1.36^{+0.13}_{-0.12}$	$1.38^{+0.23}_{-0.20}$	⋯
NGC 5585	-10.826	$-0.079^{+0.030}_{-0.030}$	$0.024^{+0.005}_{-0.004}$	$5.02^{+0.81}_{-0.70}$	$51.78^{+1.95}_{-1.94}$	$1.38^{+0.13}_{-0.12}$	$0.36^{+0.07}_{-0.06}$	⋯
NGC 5907	-10.578	$0.095^{+0.015}_{-0.014}$	$0.032^{+0.007}_{-0.006}$	$16.09^{+0.80}_{-0.76}$	$87.51^{+1.54}_{-1.87}$	$1.31^{+0.12}_{-0.11}$	$0.65^{+0.04}_{-0.04}$	⋯
NGC 5985	-10.293	$0.191^{+0.039}_{-0.035}$	$0.030^{+0.004}_{-0.003}$	$72.68^{+8.97}_{-8.02}$	$62.12^{+1.90}_{-1.89}$	$1.34^{+0.13}_{-0.11}$	$0.43^{+0.07}_{-0.06}$	$1.85^{+0.26}_{-0.23}$
NGC 6015	-10.153	$-0.088^{+0.022}_{-0.023}$	$0.032^{+0.007}_{-0.006}$	$8.07^{+0.86}_{-0.78}$	$60.87^{+1.95}_{-1.94}$	$1.37^{+0.13}_{-0.12}$	$1.68^{+0.21}_{-0.18}$	⋯
NGC 6195	-9.935	$-0.010^{+0.036}_{-0.035}$	$0.025^{+0.004}_{-0.004}$	$110.28^{+9.45}_{-8.65}$	$59.81^{+4.44}_{-4.20}$	$1.46^{+0.14}_{-0.13}$	$0.29^{+0.05}_{-0.04}$	$0.80^{+0.09}_{-0.08}$
NGC 6503	-11.156	$0.008^{+0.006}_{-0.006}$	$0.029^{+0.003}_{-0.003}$	$6.80^{+0.29}_{-0.28}$	$75.79^{+1.85}_{-1.85}$	$1.37^{+0.13}_{-0.12}$	$0.41^{+0.03}_{-0.03}$	⋯
NGC 6674	-10.613	$-0.015^{+0.019}_{-0.022}$	$0.030^{+0.007}_{-0.005}$	$37.40^{+6.20}_{-5.27}$	$52.29^{+5.50}_{-5.19}$	$1.37^{+0.13}_{-0.12}$	$1.08^{+0.33}_{-0.28}$	$1.40^{+0.59}_{-0.41}$
NGC 6789	-10.543	$-0.231^{+0.106}_{-0.107}$	$0.034^{+0.005}_{-0.005}$	$3.52^{+0.18}_{-0.17}$	$46.96^{+6.61}_{-6.42}$	$1.35^{+0.13}_{-0.12}$	$0.51^{+0.13}_{-0.10}$	⋯
NGC 6946	-10.232	$0.047^{+0.026}_{-0.027}$	$0.086^{+0.042}_{-0.028}$	$4.26^{+0.55}_{-0.49}$	$41.94^{+1.82}_{-1.81}$	$1.40^{+0.13}_{-0.12}$	$0.48^{+0.07}_{-0.06}$	$0.56^{+0.07}_{-0.06}$
NGC 7331	-10.246	$-0.075^{+0.017}_{-0.018}$	$0.109^{+0.045}_{-0.032}$	$12.28^{+0.89}_{-0.83}$	$74.95^{+1.98}_{-1.98}$	$1.34^{+0.12}_{-0.11}$	$0.41^{+0.04}_{-0.04}$	$0.63^{+0.14}_{-0.12}$
NGC 7793	-10.476	$0.265^{+0.087}_{-0.070}$	$0.077^{+0.059}_{-0.033}$	$3.59^{+0.18}_{-0.17}$	$69.24^{+5.98}_{-5.73}$	$1.45^{+0.14}_{-0.13}$	$0.33^{+0.04}_{-0.03}$	⋯
NGC 7814	-10.119	$-0.104^{+0.018}_{-0.018}$	$0.058^{+0.033}_{-0.021}$	$14.76^{+0.64}_{-0.61}$	$89.33^{+0.47}_{-0.73}$	$1.40^{+0.14}_{-0.12}$	$0.83^{+0.13}_{-0.12}$	$0.58^{+0.05}_{-0.05}$
UGC 00128	-11.228	$0.016^{+0.007}_{-0.007}$	$0.030^{+0.004}_{-0.003}$	$49.37^{+6.76}_{-5.80}$	$52.53^{+5.65}_{-4.89}$	$1.12^{+0.10}_{-0.09}$	$1.78^{+0.21}_{-0.19}$	⋯
UGC 00191	-10.736	$0.103^{+0.056}_{-0.042}$	$0.028^{+0.004}_{-0.004}$	$16.17^{+3.28}_{-2.61}$	$48.05^{+4.39}_{-4.25}$	$1.28^{+0.12}_{-0.11}$	$0.78^{+0.13}_{-0.11}$	⋯
UGC 00634	-11.252	$0.029^{+0.034}_{-0.029}$	$0.012^{+0.002}_{-0.002}$	$29.87^{+6.19}_{-4.99}$	$41.44^{+5.38}_{-4.83}$	$1.39^{+0.13}_{-0.12}$	$0.45^{+0.10}_{-0.08}$	⋯
UGC 00731	-11.329	$-0.185^{+0.390}_{-0.057}$	$0.024^{+0.004}_{-0.003}$	$5.02^{+12.66}_{-1.11}$	$56.35^{+3.65}_{-3.55}$	$1.16^{+0.14}_{-0.13}$	$0.75^{+2.32}_{-0.24}$	⋯
UGC 00891	-11.289	$-0.106^{+0.021}_{-0.024}$	$0.066^{+0.010}_{-0.009}$	$5.44^{+0.90}_{-0.76}$	$56.32^{+5.03}_{-4.91}$	$1.34^{+0.13}_{-0.12}$	$0.42^{+0.10}_{-0.08}$	⋯
UGC 01281	-11.381	$0.015^{+0.020}_{-0.018}$	$0.027^{+0.005}_{-0.004}$	$5.32^{+0.24}_{-0.23}$	$89.33^{+0.47}_{-0.73}$	$1.42^{+0.13}_{-0.12}$	$0.45^{+0.09}_{-0.08}$	⋯
UGC 02259	-10.967	$0.223^{+0.099}_{-0.071}$	$0.011^{+0.002}_{-0.002}$	$16.03^{+3.25}_{-2.65}$	$44.36^{+2.74}_{-2.71}$	$1.30^{+0.12}_{-0.11}$	$0.89^{+0.16}_{-0.13}$	⋯
UGC 02487	-10.562	$0.100^{+0.012}_{-0.012}$	$0.024^{+0.004}_{-0.003}$	$73.77^{+9.09}_{-8.03}$	$46.14^{+3.57}_{-3.42}$	$1.49^{+0.15}_{-0.13}$	$0.58^{+0.12}_{-0.10}$	$0.59^{+0.10}_{-0.09}$
UGC 02885	-10.646	$0.009^{+0.026}_{-0.025}$	$0.023^{+0.003}_{-0.003}$	$81.67^{+6.86}_{-6.32}$	$66.70^{+3.60}_{-3.53}$	$1.44^{+0.14}_{-0.13}$	$0.44^{+0.06}_{-0.06}$	$0.92^{+0.11}_{-0.10}$
UGC 02916	-9.938	$0.295^{+0.090}_{-0.074}$	$0.015^{+0.002}_{-0.002}$	$58.36^{+6.36}_{-5.64}$	$58.52^{+3.95}_{-3.78}$	$1.39^{+0.13}_{-0.12}$	$1.10^{+0.15}_{-0.13}$	$0.43^{+0.05}_{-0.04}$
UGC 02953	-9.497	$-0.006^{+0.006}_{-0.006}$	$0.021^{+0.004}_{-0.003}$	$13.51^{+0.86}_{-0.76}$	$64.56^{+3.05}_{-3.03}$	$1.51^{+0.15}_{-0.13}$	$0.57^{+0.03}_{-0.02}$	$0.58^{+0.02}_{-0.02}$
UGC 03205	-9.813	$0.004^{+0.019}_{-0.019}$	$0.013^{+0.002}_{-0.002}$	$42.44^{+4.52}_{-4.07}$	$70.75^{+3.59}_{-3.54}$	$1.33^{+0.12}_{-0.11}$	$0.63^{+0.09}_{-0.08}$	$1.30^{+0.14}_{-0.13}$
UGC 03546	-10.141	$0.020^{+0.022}_{-0.023}$	$0.035^{+0.004}_{-0.004}$	$24.38^{+3.30}_{-2.88}$	$60.82^{+4.29}_{-4.19}$	$1.40^{+0.13}_{-0.12}$	$0.58^{+0.10}_{-0.08}$	$0.43^{+0.06}_{-0.05}$
UGC 03580	-10.262	$-0.045^{+0.011}_{-0.011}$	$0.025^{+0.006}_{-0.005}$	$15.18^{+1.38}_{-1.24}$	$67.11^{+3.58}_{-3.54}$	$1.51^{+0.14}_{-0.13}$	$0.47^{+0.06}_{-0.05}$	$0.15^{+0.02}_{-0.02}$
UGC 04278	-11.272	$-0.164^{+0.033}_{-0.038}$	$0.011^{+0.002}_{-0.002}$	$5.89^{+0.97}_{-0.89}$	$88.01^{+1.40}_{-2.18}$	$1.38^{+0.13}_{-0.12}$	$0.37^{+0.08}_{-0.07}$	⋯
UGC 04325	-10.656	$0.354^{+0.100}_{-0.125}$	$0.008^{+0.002}_{-0.001}$	$13.64^{+2.31}_{-2.01}$	$43.99^{+2.73}_{-2.69}$	$1.25^{+0.12}_{-0.11}$	$1.07^{+0.20}_{-0.17}$	⋯
UGC 04483	-11.284	$0.153^{+0.061}_{-0.049}$	$0.016^{+0.002}_{-0.002}$	$3.37^{+0.31}_{-0.29}$	$58.97^{+2.94}_{-2.95}$	$1.37^{+0.13}_{-0.12}$	$0.48^{+0.11}_{-0.09}$	⋯
UGC 04499	-11.102	$0.121^{+0.107}_{-0.076}$	$0.015^{+0.002}_{-0.002}$	$13.43^{+3.56}_{-2.69}$	$51.41^{+2.89}_{-2.88}$	$1.38^{+0.13}_{-0.12}$	$0.49^{+0.09}_{-0.08}$	⋯
UGC 05005	-11.701	$0.149^{+0.125}_{-0.087}$	$0.032^{+0.003}_{-0.002}$	$51.72^{+10.54}_{-8.86}$	$52.66^{+8.76}_{-8.71}$	$1.42^{+0.14}_{-0.13}$	$0.39^{+0.08}_{-0.07}$	⋯
UGC 05253	-9.707	$0.058^{+0.009}_{-0.009}$	$0.026^{+0.003}_{-0.003}$	$20.87^{+2.22}_{-1.94}$	$52.15^{+3.05}_{-2.98}$	$1.40^{+0.13}_{-0.12}$	$0.30^{+0.04}_{-0.03}$	$0.39^{+0.03}_{-0.03}$
UGC 05414	-11.019	$0.083^{+0.132}_{-0.095}$	$0.019^{+0.003}_{-0.002}$	$9.03^{+2.73}_{-2.07}$	$55.52^{+2.98}_{-2.96}$	$1.40^{+0.14}_{-0.12}$	$0.42^{+0.10}_{-0.08}$	⋯
UGC 05716	-11.440	$0.091^{+0.035}_{-0.028}$	$0.020^{+0.005}_{-0.004}$	$22.21^{+3.80}_{-3.08}$	$65.58^{+7.60}_{-7.10}$	$1.25^{+0.11}_{-0.10}$	$0.86^{+0.10}_{-0.09}$	⋯
UGC 05721	-10.917	$0.048^{+0.034}_{-0.030}$	$0.021^{+0.003}_{-0.003}$	$10.10^{+1.61}_{-1.36}$	$67.74^{+4.28}_{-4.21}$	$1.39^{+0.14}_{-0.12}$	$0.51^{+0.11}_{-0.09}$	⋯
UGC 05750	-11.469	$0.151^{+0.097}_{-0.067}$	$0.048^{+0.010}_{-0.008}$	$62.77^{+12.27}_{-10.27}$	$72.30^{+7.85}_{-7.93}$	$1.37^{+0.13}_{-0.12}$	$0.55^{+0.13}_{-0.11}$	⋯
UGC 05764	-11.191	$0.390^{+0.073}_{-0.086}$	$0.046^{+0.053}_{-0.025}$	$14.73^{+1.98}_{-1.80}$	$74.46^{+6.79}_{-6.70}$	$1.10^{+0.10}_{-0.09}$	$2.66^{+0.33}_{-0.29}$	⋯
UGC 05829	-11.263	$0.128^{+0.237}_{-0.163}$	$0.743^{+0.214}_{-0.166}$	$6.81^{+1.96}_{-1.62}$	$41.90^{+9.07}_{-9.29}$	$1.27^{+0.12}_{-0.11}$	$0.69^{+0.18}_{-0.17}$	⋯
UGC 05918	-11.581	$0.046^{+0.087}_{-0.064}$	$0.020^{+0.003}_{-0.002}$	$7.47^{+2.47}_{-1.82}$	$48.80^{+4.86}_{-4.87}$	$1.33^{+0.13}_{-0.12}$	$0.59^{+0.15}_{-0.12}$	⋯
UGC 05986	-10.836	$-0.016^{+0.037}_{-0.036}$	$0.033^{+0.009}_{-0.007}$	$12.87^{+2.34}_{-1.97}$	$88.04^{+1.37}_{-2.13}$	$1.49^{+0.15}_{-0.13}$	$0.37^{+0.08}_{-0.06}$	⋯
UGC 06399	-11.019	$-0.002^{+0.051}_{-0.044}$	$0.009^{+0.002}_{-0.001}$	$18.58^{+2.52}_{-2.21}$	$75.24^{+1.98}_{-1.98}$	$1.37^{+0.13}_{-0.12}$	$0.54^{+0.12}_{-0.10}$	⋯
UGC 06446	-11.165	$0.154^{+0.093}_{-0.067}$	$0.019^{+0.003}_{-0.002}$	$17.45^{+3.84}_{-3.02}$	$54.18^{+2.79}_{-2.78}$	$1.28^{+0.12}_{-0.11}$	$0.91^{+0.15}_{-0.12}$	⋯
UGC 06614	-10.336	$-0.066^{+0.035}_{-0.036}$	$0.026^{+0.004}_{-0.003}$	$82.51^{+8.17}_{-7.43}$	$31.00^{+3.15}_{-2.82}$	$1.42^{+0.14}_{-0.12}$	$0.47^{+0.11}_{-0.09}$	$0.57^{+0.13}_{-0.11}$
UGC 06667	-11.287	$-0.117^{+0.022}_{-0.023}$	$0.027^{+0.005}_{-0.004}$	$15.64^{+1.82}_{-1.66}$	$88.80^{+0.75}_{-0.91}$	$1.31^{+0.12}_{-0.11}$	$0.52^{+0.14}_{-0.11}$	⋯
UGC 06786	-10.094	$-0.028^{+0.012}_{-0.012}$	$0.027^{+0.005}_{-0.004}$	$46.17^{+4.36}_{-3.99}$	$68.02^{+2.70}_{-2.70}$	$1.49^{+0.14}_{-0.13}$	$0.36^{+0.05}_{-0.04}$	$0.42^{+0.04}_{-0.04}$

Table 2
(Continued)

Galaxy	$\langle x_0 \rangle$	e	$e_{\rm env}$	D (Mpc)	i (°)	$\Upsilon_{\rm gas}$	$\Upsilon_{\rm disk}$	$\Upsilon_{\rm bulge}$
UGC 06787	-10.632	$0.302^{+0.029}_{-0.025}$	$0.028^{+0.005}_{-0.004}$	$106.11^{+8.22}_{-7.52}$	$72.66^{+2.51}_{-2.50}$	$3.25^{+0.26}_{-0.25}$	$0.17^{+0.01}_{-0.01}$	$0.08^{+0.01}_{-0.01}$
UGC 06818	-11.263	$-0.001^{+0.040}_{-0.035}$	$0.031^{+0.004}_{-0.004}$	$15.71^{+2.23}_{-1.93}$	$74.65^{+3.04}_{-3.03}$	$1.42^{+0.14}_{-0.13}$	$0.31^{+0.07}_{-0.06}$	⋯
UGC 06917	-10.831	$0.001^{+0.047}_{-0.043}$	$0.007^{+0.002}_{-0.001}$	$17.98^{+2.23}_{-1.97}$	$56.50^{+1.95}_{-1.95}$	$1.36^{+0.13}_{-0.12}$	$0.55^{+0.09}_{-0.08}$	⋯
UGC 06923	-10.790	$0.042^{+0.092}_{-0.072}$	$0.022^{+0.003}_{-0.003}$	$17.32^{+2.36}_{-2.06}$	$65.05^{+1.99}_{-2.00}$	$1.38^{+0.13}_{-0.12}$	$0.45^{+0.10}_{-0.08}$	⋯
UGC 06930	-11.033	$0.259^{+0.130}_{-0.106}$	$0.034^{+0.005}_{-0.005}$	$18.30^{+2.35}_{-2.10}$	$38.76^{+3.84}_{-3.80}$	$1.36^{+0.13}_{-0.12}$	$0.58^{+0.11}_{-0.09}$	⋯
UGC 06983	-10.952	$0.059^{+0.040}_{-0.036}$	$0.034^{+0.006}_{-0.005}$	$19.85^{+2.31}_{-2.06}$	$49.43^{+0.98}_{-0.99}$	$1.33^{+0.13}_{-0.11}$	$0.77^{+0.11}_{-0.10}$	⋯
UGC 07089	-11.166	$0.102^{+0.073}_{-0.055}$	$0.033^{+0.005}_{-0.005}$	$17.11^{+2.44}_{-2.12}$	$80.16^{+2.97}_{-2.98}$	$1.40^{+0.14}_{-0.12}$	$0.40^{+0.09}_{-0.07}$	⋯
UGC 07125	-11.386	$0.132^{+0.075}_{-0.050}$	$0.007^{+0.002}_{-0.002}$	$13.56^{+3.20}_{-2.31}$	$87.98^{+1.42}_{-2.19}$	$1.27^{+0.12}_{-0.11}$	$0.69^{+0.11}_{-0.09}$	⋯
UGC 07151	-10.712	$0.163^{+0.071}_{-0.056}$	$0.029^{+0.005}_{-0.004}$	$6.97^{+0.34}_{-0.32}$	$88.04^{+1.38}_{-2.14}$	$1.35^{+0.13}_{-0.12}$	$0.71^{+0.10}_{-0.09}$	⋯
UGC 07232	-10.680	$-0.024^{+0.104}_{-0.082}$	$0.024^{+0.004}_{-0.003}$	$2.82^{+0.17}_{-0.16}$	$59.49^{+4.99}_{-4.97}$	$1.37^{+0.13}_{-0.12}$	$0.46^{+0.12}_{-0.09}$	⋯
UGC 07261	-11.097	$0.258^{+0.152}_{-0.143}$	$0.028^{+0.004}_{-0.003}$	$12.39^{+3.13}_{-2.51}$	$41.87^{+6.87}_{-6.43}$	$1.36^{+0.13}_{-0.12}$	$0.49^{+0.10}_{-0.08}$	⋯
UGC 07323	-10.898	$0.150^{+0.180}_{-0.140}$	$0.024^{+0.004}_{-0.004}$	$8.41^{+2.19}_{-1.91}$	$48.55^{+2.89}_{-2.90}$	$1.41^{+0.13}_{-0.12}$	$0.43^{+0.10}_{-0.08}$	⋯
UGC 07399	-10.920	$-0.024^{+0.041}_{-0.040}$	$0.018^{+0.004}_{-0.003}$	$14.30^{+2.56}_{-2.15}$	$57.55^{+2.83}_{-2.79}$	$1.38^{+0.13}_{-0.12}$	$0.61^{+0.13}_{-0.11}$	⋯
UGC 07524	-11.181	$0.169^{+0.064}_{-0.052}$	$0.032^{+0.008}_{-0.006}$	$4.73^{+0.24}_{-0.23}$	$49.80^{+2.79}_{-2.77}$	$1.24^{+0.11}_{-0.11}$	$0.90^{+0.14}_{-0.12}$	⋯
UGC 07559[a]	⋯	$0.229^{+0.092}_{-0.066}$	$0.022^{+0.004}_{-0.004}$	$4.98^{+0.25}_{-0.24}$	$61.79^{+2.94}_{-2.96}$	$1.37^{+0.13}_{-0.12}$	$0.48^{+0.12}_{-0.10}$	⋯
UGC 07577[a]	⋯	$0.429^{+0.051}_{-0.079}$	$0.038^{+0.003}_{-0.003}$	$2.55^{+0.13}_{-0.12}$	$62.77^{+2.95}_{-2.93}$	$1.32^{+0.12}_{-0.11}$	$0.42^{+0.08}_{-0.07}$	⋯
UGC 07603	-10.997	$-0.068^{+0.033}_{-0.034}$	$0.032^{+0.003}_{-0.003}$	$4.69^{+0.81}_{-0.69}$	$78.38^{+2.94}_{-2.94}$	$1.39^{+0.13}_{-0.12}$	$0.44^{+0.10}_{-0.08}$	⋯
UGC 07690	-10.824	$0.249^{+0.136}_{-0.111}$	$0.027^{+0.003}_{-0.003}$	$8.91^{+1.92}_{-1.60}$	$45.30^{+4.32}_{-4.18}$	$1.36^{+0.13}_{-0.12}$	$0.53^{+0.12}_{-0.09}$	⋯
UGC 07866[a]	⋯	$0.230^{+0.124}_{-0.094}$	$0.036^{+0.007}_{-0.006}$	$4.58^{+0.23}_{-0.22}$	$47.67^{+4.57}_{-4.64}$	$1.35^{+0.13}_{-0.12}$	$0.53^{+0.13}_{-0.10}$	⋯
UGC 08286	-10.832	$0.021^{+0.015}_{-0.014}$	$0.023^{+0.004}_{-0.004}$	$6.60^{+0.21}_{-0.20}$	$88.10^{+1.34}_{-2.07}$	$1.32^{+0.12}_{-0.11}$	$1.14^{+0.09}_{-0.08}$	⋯
UGC 08490	-11.162	$0.035^{+0.016}_{-0.015}$	$0.026^{+0.005}_{-0.004}$	$5.21^{+0.47}_{-0.43}$	$55.39^{+2.57}_{-2.53}$	$1.37^{+0.13}_{-0.12}$	$0.67^{+0.11}_{-0.09}$	⋯
UGC 08550	-11.251	$0.002^{+0.027}_{-0.026}$	$0.025^{+0.004}_{-0.003}$	$6.53^{+1.01}_{-0.86}$	$88.00^{+1.40}_{-2.17}$	$1.28^{+0.12}_{-0.11}$	$0.72^{+0.13}_{-0.11}$	⋯
UGC 08699	-10.120	$-0.010^{+0.023}_{-0.024}$	$0.040^{+0.014}_{-0.010}$	$37.47^{+4.57}_{-4.05}$	$80.75^{+5.30}_{-5.90}$	$1.38^{+0.13}_{-0.12}$	$0.63^{+0.12}_{-0.10}$	$0.68^{+0.08}_{-0.07}$
UGC 08837	-11.296	$0.243^{+0.079}_{-0.060}$	$0.024^{+0.005}_{-0.004}$	$7.25^{+0.36}_{-0.34}$	$80.76^{+4.46}_{-4.66}$	$1.44^{+0.13}_{-0.12}$	$0.40^{+0.08}_{-0.07}$	⋯
UGC 09037	-10.734	$-0.012^{+0.038}_{-0.036}$	$0.030^{+0.006}_{-0.005}$	$73.65^{+6.81}_{-6.22}$	$63.86^{+4.85}_{-4.73}$	$1.45^{+0.14}_{-0.13}$	$0.22^{+0.03}_{-0.03}$	⋯
UGC 09133	-9.810	$0.043^{+0.007}_{-0.007}$	$0.042^{+0.011}_{-0.009}$	$35.41^{+3.55}_{-3.03}$	$64.82^{+4.56}_{-4.40}$	$1.50^{+0.15}_{-0.13}$	$0.83^{+0.09}_{-0.09}$	$0.72^{+0.04}_{-0.04}$
UGC 09992[a]	⋯	$0.361^{+0.099}_{-0.143}$	$0.033^{+0.007}_{-0.006}$	$9.34^{+2.49}_{-1.95}$	$34.77^{+6.19}_{-5.66}$	$1.34^{+0.13}_{-0.12}$	$0.50^{+0.12}_{-0.10}$	⋯
UGC 10310	-11.108	$0.285^{+0.139}_{-0.144}$	$0.044^{+0.009}_{-0.008}$	$16.04^{+3.73}_{-3.12}$	$40.49^{+4.80}_{-4.66}$	$1.31^{+0.12}_{-0.11}$	$0.66^{+0.14}_{-0.11}$	⋯
UGC 11455	-9.898	$-0.033^{+0.025}_{-0.026}$	$0.027^{+0.005}_{-0.004}$	$72.36^{+8.14}_{-7.33}$	$89.33^{+0.47}_{-0.73}$	$1.42^{+0.14}_{-0.12}$	$0.46^{+0.07}_{-0.06}$	⋯
UGC 11557	-10.904	$0.350^{+0.108}_{-0.172}$	$0.025^{+0.005}_{-0.004}$	$17.98^{+4.18}_{-3.36}$	$32.83^{+5.63}_{-5.21}$	$1.40^{+0.13}_{-0.12}$	$0.35^{+0.09}_{-0.07}$	⋯
UGC 11820	-11.305	$-0.014^{+0.019}_{-0.019}$	$0.039^{+0.009}_{-0.008}$	$12.15^{+3.01}_{-2.29}$	$44.26^{+6.72}_{-5.86}$	$1.20^{+0.11}_{-0.10}$	$0.98^{+0.15}_{-0.13}$	⋯
UGC 11914	-9.346	$-0.396^{+0.052}_{-0.050}$	$0.031^{+0.005}_{-0.004}$	$8.80^{+1.43}_{-1.19}$	$48.85^{+3.68}_{-3.57}$	$1.42^{+0.14}_{-0.13}$	$0.30^{+0.05}_{-0.04}$	$0.89^{+0.12}_{-0.11}$
UGC 12506	-10.508	$0.241^{+0.064}_{-0.053}$	$0.033^{+0.006}_{-0.005}$	$117.17^{+10.52}_{-9.67}$	$86.11^{+2.48}_{-3.11}$	$1.43^{+0.14}_{-0.13}$	$1.04^{+0.13}_{-0.11}$	⋯
UGC 12632	-11.304	$0.277^{+0.122}_{-0.099}$	$0.028^{+0.004}_{-0.004}$	$13.03^{+2.59}_{-2.35}$	$49.17^{+2.78}_{-2.77}$	$1.25^{+0.11}_{-0.10}$	$1.05^{+0.16}_{-0.14}$	⋯
UGC 12732	-11.361	$0.136^{+0.093}_{-0.062}$	$0.029^{+0.005}_{-0.004}$	$13.22^{+3.32}_{-2.55}$	$48.25^{+4.97}_{-4.78}$	$1.26^{+0.12}_{-0.11}$	$0.86^{+0.12}_{-0.10}$	⋯
UGC A442	-11.259	$-0.050^{+0.012}_{-0.013}$	$0.026^{+0.005}_{-0.004}$	$4.20^{+0.21}_{-0.20}$	$51.17^{+3.93}_{-3.59}$	$1.29^{+0.12}_{-0.11}$	$0.45^{+0.11}_{-0.09}$	⋯
UGC A444[a]	⋯	$0.063^{+0.026}_{-0.023}$	$0.028^{+0.005}_{-0.004}$	$0.95^{+0.05}_{-0.05}$	$78.77^{+3.86}_{-3.88}$	$1.25^{+0.12}_{-0.11}$	$0.57^{+0.15}_{-0.12}$	⋯

Notes. See Figure 1 and Section 2.2 for the definition of x_0. Here $\langle x_0 \rangle$ represents the median of x_0 for the rotation velocities with signal-to-noise ratios >10.
[a] For these galaxies no circular velocities have signal-to-noise ratios >10. These galaxies are not included in our statistical analyses of EFE.

ORCID iDs

Kyu-Hyun Chae https://orcid.org/0000-0002-6016-2736
Federico Lelli https://orcid.org/0000-0002-9024-9883
Harry Desmond https://orcid.org/0000-0003-0685-9791
Stacy S. McGaugh https://orcid.org/0000-0002-9762-0980
Pengfei Li https://orcid.org/0000-0002-6707-2581
James M. Schombert https://orcid.org/0000-0003-2022-1911

References

Bacchini, C., Fraternali, F., Iorio, G., & Pezzulli, G. 2019, A&A, 622, A64
Baumgardt, H., Grebel, E. K., & Kroupa, P. 2005, MNRAS, 359, L1
Bekenstein, J., & Milgrom, M. 1984, ApJ, 286, 7
Brada, R., & Milgrom, M. 1995, MNRAS, 276, 453
Bullock, J. S., & Boylan-Kolchin, M. 2017, ARA&A, 55, 343
Chae, K.-H., Bernardi, M., Sheth, R. K., & Gong, I.-T. 2019, ApJ, 877, 18
Desmond, H. 2017, MNRAS, 464, 4160
Desmond, H., Ferreira, P. G., Lavaux, G., & Jasche, J. 2018, MNRAS, 474, 3152
Di Cintio, A., & Lelli, F. 2016, MNRAS, 456, L127
Diemer, B., & Kravtsov, A. V. 2015, ApJ, 799, 108
Famaey, B., & Binney, J. 2005, MNRAS, 363, 603
Famaey, B., & McGaugh, S. S. 2012, LRR, 15, 10
Famaey, B., McGaugh, S. S., & Milgrom, M. 2018, MNRAS, 480, 473
Fattahi, A., Navarro, J. F., Frenk, C. S., et al. 2018, MNRAS, 476, 3816
Foreman-Mackey, D., Hogg, D. W., Lang, D., & Goodman, J. 2013, PASP, 125, 306
Frank, M. J., Hilker, M., Baumgardt, H., et al. 2012, MNRAS, 423, 2917
Frenk, C. S., & White, S. D. M. 2012, AnP, 524, 507
Garaldi, E., Romano-Díaz, E., Porciani, C., & Pawlowski, M. S. 2019, PhRvL, 120, 261301
Haghi, H., Baumgardt, H., & Kroupa, P. 2011, A&A, 527, A33
Haghi, H., Baumgardt, H., Kroupa, P., et al. 2009, MNRAS, 395, 1549
Haghi, H., Bazkiaei, A. E., Zonoozi, A. H., & Kroupa, P. 2016, MNRAS, 458, 4172
Haghi, H., Kroupa, P., Banik, I., et al. 2019, MNRAS, 487, 2441
Hernandez, X., Cortés, R. A. M., Allen, C., & Scarpa, R. 2019, IJMPD, 28, 1950101

Hernandez, X., Jiménez, M. A., & Allen, C. 2012, EPJC, 72, 1884
Jordi, K., Grebel, E. K., Hilker, M., et al. 2009, AJ, 137, 4586
Keller, B. W., & Wadsley, J. W. 2017, ApJL, 835, L17
King, I. 1962, AJ, 67, 471
Kravtsov, A. V., Vikhlinin, A. A., & Meshcheryakov, A. V. 2018, AstL, 44, 8
Kroupa, P. 2015, CaJPh, 93, 169
Kroupa, P., Famaey, B., Boer, K. S., et al. 2010, A&A, 523, A32
Kroupa, P., Haghi, H., Javanmardi, B., et al. 2018, Natur, 561, E4
Lavaux, G., & Hudson, M. J. 2011, MNRAS, 416, 2840
Lavaux, G., & Jasche, J. 2016, MNRAS, 455, 3169
Lelli, F., Duc, P. A., Brinks, E., et al. 2015, A&A, 584, A113
Lelli, F., McGaugh, S. S., & Schombert, J. M. 2016, AJ, 152, 157
Lelli, F., McGaugh, S. S., Schombert, J. M., & Pawlowski, M. S. 2017, ApJ, 836, 152
Li, P., Lelli, F., McGaugh, S., & Schombert, J. 2018, A&A, 615, 70
Ludlow, A., Benítez-Llambay, A., Schaller, M., et al. 2017, PhRvL, 118, 161103
McGaugh, S. S. 2015, CaJPH, 93, 250
McGaugh, S. S. 2020, Galax, 8, 35
McGaugh, S. S., Lelli, F., & Schombert, J. M. 2016, PhRvL, 117, 201101
McGaugh, S. S., Lelli, F., & Schombert, J. M. 2020, RNAAS, 4, 45
McGaugh, S. S., & Milgrom, M. 2013a, ApJ, 766, 22
McGaugh, S. S., & Milgrom, M. 2013b, ApJ, 775, 139
McGaugh, S. S., & Wolf, J. 2010, ApJ, 722, 248
Milgrom, M. 1983, ApJ, 270, 365
Milgrom, M. 1994, AnPhy, 229, 384
Müller, O., Famaey, B., & Zhao, H. 2019, A&A, 623, A36
Müller, O., Pawlowski, M. S., Jerjen, H., & Lelli, F. 2018, Sci, 359, 534
Navarro, J. F., Benítez-Llambay, A., Fattahi, A., et al. 2017, MNRAS, 471, 1841
Navarro, J. F., Frenk, C. S., & White, S. D. M. 1997, ApJ, 490, 493
Peebles, P. J. E. 2012, ARA&A, 50, 1
Pittordis, C., & Sutherland, W. 2019, MNRAS, 488, 4740
Sanders, R. H., & McGaugh, S. S. 2002, ARA&A, 40, 263
Schombert, J. M., McGaugh, S. S., & Lelli, F. 2019, MNRAS, 483, 1496
Skordis, C., & Złośnik, T. 2020, arXiv:2007.00082
Tenneti, A., Mao, Y.-Y., Croft, R. A. C., et al. 2018, MNRAS, 474, 3125
van Dokkum, P., Danieli, S., Abraham, R., et al. 2019, ApJL, 874, L5
van Dokkum, P., Danieli, S., Cohen, Y., et al. 2018, Natur, 555, 629
Will, C. M. 2014, LRR, 17, 4
Wu, X., & Kroupa, P. 2015, MNRAS, 446, 330